

**A MM/QM APPROACH TO SIMULATING
ELECTRON/HOLE SEPARATION KINETICS OF
ORGANIC POLYMERS BULK-HETEROJUNCTIONS**

A Dissertation Presented to
the Faculty of the Department of Chemistry
University of Houston

In Partial Fulfillment
of the Requirements for the Degree
Doctor of Philosophy

By
Allen Kelley
December 2016

A MM/QM APPROACH TO SIMULATING
ELECTRON/HOLE SEPARATION KINETICS OF
ORGANIC POLYMERS BULK-HETEROJUNCTIONS

Allen Kelley

APPROVED:

Eric Bittner, Chairman
Dept. of Chemistry

Vassiliy Lubchenko
Dept. of Chemistry

Margaret Cheung
Dept. of Physics

Shoujun Xu
Dept. of Chemistry

Scott Gilbertson
Dept. of Chemistry

Dean, College of Natural Sciences and Mathematics

Acknowledgments

I would first and foremost like to thank my grandmother Jan Kelley for believing in me and helping me transition into junior college. I would like to thank my wife Alma Kelley and kids Alexa and Albert Kelley for being understanding and allowing me to pursue my dreams. I would like to thank my wife's family helping and providing a stable base for which I could rely on during my studies. Growing up disadvantaged, I understand that finishing my degree will partially fulfill the dreams of countless people around me. To these people I say thank you for your kind words and support. To my P.I. Dr. Eric Bittner, thank you for your support. I know that I am a handful and not an easy person to get a handle on, so thank you for your patience and guidance through the years. To all of my friends Kush Patel, Vlad Lankevich, Robert Paredez and Xumno Yang thank you for making graduate school a fun a lively place day in and day out.

**A MM/QM APPROACH TO SIMULATING
ELECTRON/HOLE SEPARATION KINETICS OF
ORGANIC POLYMERS BULK-HETEROJUNCTIONS**

An Abstract of a Dissertation
Presented to
the Faculty of the Department of Chemistry
University of Houston

In Partial Fulfillment
of the Requirements for the Degree
Doctor of Philosophy

By
Allen Kelley
December 2016

Abstract

We investigate the electronic dynamics of model organic photovoltaic (OPV) system consisting of polyphenylene vinylene (PPV) oligomers and [6,6]-phenyl C61-butyric acid methylester (PCBM) blend using a mixed molecular mechanics/quantum mechanics (MM/QM) approach. The π -MDX code is introduced and a methodology that allows the quantum treatment of the π systems of large clusters of molecules near the interface is developed. Using a heuristic model that connects energy gap fluctuations to the average electronic couplings and decoherence times, we provide an estimate of the state-to-state internal conversion rates within the manifold of the lowest few electronic excitations. We find that the lowest few excited states of a model interface are rapidly mixed by C=C bond fluctuations and low frequency torsional modes such that the system can sample both intermolecular charge-transfer and charge-separated electronic configurations on a time scale of 20fs. We show that the electronic dynamics of the OPV are dramatically altered by varying the positions of the molecules simulated at the interface. Our simulations support an emerging picture of carrier generation in OPV systems in which interfacial electronic states can rapidly decay into charge-separated and current producing states via coupling to vibronic degrees of freedom.

Contents

1	Introduction	1
1.1	General Introduction	1
1.2	Photovoltaic Cells	2
1.3	Bulk Heterojunction	6
1.4	History of Computational Methods Employed to Study Conjugated Polymers	12
1.4.1	Hückel Theory	13
1.4.2	1.4.2 Example of Hückel Model on (1,3)-butadiene	14
1.5	The MM/QM Approach	15
1.6	Dissertation Overview	19
2	Methods	21
2.1	Introduction	21
2.2	Pariser-Parr-Pople Hamiltonian	23
2.3	Configuration Interaction (Singles)	30
3	Simulation	36
3.1	Introduction	36
3.2	TINKER XYZ and Key files	37
3.3	Creation of Simulation Cells and Solvent Boxes	38

3.4	Generating the Fock Matrix	41
3.5	Generating the CIS Matrix	45
3.6	Then Bond Charge Matrix and MM	48
4	Structural Fluctuations and Environmental Noise in the Electron/Hole Separation Kinetics at Organic Polymer Bulk-Heterojunction Interfaces	51
4.1	Introduction	52
4.2	A Model Two Level System	56
4.3	Noise Averaged Kinetics	58
4.4	Methods	64
4.5	Results	67
4.6	Conclusions	71
5	Quantum simulations of charge-separation at a model donor-acceptor interface: role of delocalization and local packing	77
5.1	Introduction	77
5.2	Methods	79
5.3	Results	82
5.4	Conclusions	90
	Bibliography	92

List of Figures

1.1	Chemical structures of common conjugated polymers: (a) polyacetylene is the simplest conjugated polymer; (b) polythiophene (PT); (c) poly(thienylenevinylene); (d) poly(p-phenylene) (PPP); (e) poly(p-phenylenevinylene) (PPV); and (f) polyfluorene (PFO).	3
1.2	The National Renewable Energy Laboratory maintains this plot of the highest confirmed conversion efficiencies for research cells, from 1976 to the present, for a range of photovoltaic technologies. The different colors represent different families of semiconductors, with the red representing organic photovoltaic cells. The most recent world record for each technology is highlighted along the right edge in a colored flag that contains the efficiency and symbol of the technology. This plot is courtesy of the National Renewable Energy Laboratory, Golden, CO. [4]	4
1.3	Schematic diagram of a bulk heterojunction. The red represents the donor regions while the blue represents the acceptor regions. They are blended thereby increasing the interfacial surface area and the probability of exciton formation in the vicinity of the interface. The charges still require a pathway to the electrodes leading to greater sensitivity to the interfacial morphology. The exciton formed inside the bulk shown by the electron/hole pair (1), migrates to the interface where it will separate. The resulting charge transfer state (2), must overcome the Coulomb attraction and migrate away from the interface (3).	7

1.4	Jablonski diagram showing relative energetic positions of excited states in a bulk-heterojunction system. The discrete states on the left are assumed to be localized excitons or charge-transfer states while the polaron states are assumed to be a quasi-continuum of mobile charge-separated states within the bulk. The latter of these are presumed to be responsible for producing photocurrent from a given device.	8
1.5	The energy levels and orbitals for (1,3)-butadiene, generated using the Hückel model. The energies are found by solving the roots of the fourth order polynomial generated by taking the determinant of the adjacency matrix.	16
2.1	The Hartree-Fock ground state $ \Psi_0\rangle$ and Configuration Interaction Singlet excited state determents $ \Psi_a^r\rangle$	33
3.1	This is an example of the first page of a <code>TINKER.xyz</code> file. The first row shows the total number of atoms and the name of the molecules in file. The first column represents the atom number. The second column is the atom symbol. The third, forth, and fifth column are the x, y, and z components of the atom. The sixth column is the MM3 atom type. The last columns are the connectivity of the atoms.	38
3.2	This is an example of a <code>TINKER.key</code> file. The first row contains the keyword <code>parameters</code> , this tells TINKER the path to the parameters file for the simulation. The keyword, <code>pisystem</code> tells TINKER which atom number in the <code>.xyz</code> file are going to be used for the π -system atoms. The next keywords, <code>*-AXIS</code> give the initial dimensions of the solvent box used for the <code>.xyz</code> file.	39
3.3	Snapshot of the three MD simulation cells: A, B, and C. A and B contain 30 PCBM molecules and 50 PPV oligomers following equilibration at 100 k and 1 ATM of pressure. C contains 50 PCBM molecules and 25 PPV oligomers following equilibration at 100 K and 1 ATM of pressure. The red and blue highlighted molecules denote the π -active units in our system.	42

3.4	The π -active region is shown in the 5×5 bulk PPV portion. The non- π -active PCBM solvent molecules have been removed, showing how the bulk PPV region reacted to the procedure for creation of a simulation cell. The picture is centered on the central blue PPV molecule, looking directly down its axis. The molecules with blue spheres (PPV) represent donor molecules while the molecule with red spheres (PCBM) represent acceptor molecule.	43
3.5	These graphs show a plot of how the local π -bond order affects the bond stretch force constant and the equilibrium bond lengths of the system. They are generated by manually changing the value of $P(i)$ in Equations 3.10 and 3.11 for ethylene. The values shown are the actual values for the new bond order and force constant that are feed into the MM portion of π -MDX. The equilibrium bond lengths and force constants found in the MM3 parameter set are shown by the large A's. Experimental values for the bond lengths and force constants [54] are shown as large B near the structure of the molecule they where taken from.	50
4.1	A two level system between states $ 1\rangle$ and $ 2\rangle$ with an average energy gap Δ_0 . The energy gap is given by Δ where λ is the coupling between $ 1\rangle$ and $ 2\rangle$	57
4.2	Snapshot of the MD simulation cell containing 50 PCBM molecules and 25 PPV oligomers following equilibration at 100 K and 1 ATM of pressure. The blue and red highlighted molecules denote the π -active donor/acceptor units in our system.	65
4.3	Single CI (CIS) energies for the first 200 fs following excitation to the lowest CIS state. Throughout the simulation, the lowest lying state (in blue) remained populated and varied in character from excitonic to charge-separated. Labels A-E refer to the configurations shown in Figure 4.4.	68

4.4	Sequence of states following initial excitation. In this particular simulation, the initial excited state population was localized on the PCBM. This population rapidly dissociates into charge-transfer and then charge-separated configurations within 100-150 fs. This scenario appears to be a ubiquitous feature of our simulations indicating that fluctuations alone can carry the system from a localized charge-transfer state to charge-separated states, eventually to current-producing polaron states.	73
4.5	Histogram distribution of the five lowest excitation energy levels over a 50,000 ps simulation. Throughout the simulation, the lowest lying state (in blue) remained populated and varied in character from excitonic to charge-separated.	74
4.6	A 6 fs time history from 51 to 56 fs of the first excited CI state is shown in Figure 4.3. This series resides around an avoided crossing between the first and second excited state. Showing how a CT state at the interface can evolve into exciton states farther into the bulk around one avoided crossing point. After the excited states diverge, the exciton in the bulk collapses back into an exciton localized on the PCBM.	75
4.7	Histogram of energy gaps between the first excited and higher-lying excited states. Gold: 1 → 2, blue: 1 → 3, green: 1 → 4, and red: 1 → 5.	76
5.1	The dominant electronic configurations from simulation A (Bottom) and B (Top) as shown in Figure 3.3. The red and blue numbers denote the electron/hole density as a percent on the indicated molecule. The states correspond to the x axis in Figure 5.2. The four snapshots shown represent typical configurations for our systems. The top pictures from left to right present an exciton located on the PCBM molecule and a charge transfer configuration. The bottom pictures from left to right show a charge separated configuration and a partly de-localized configuration.	83
5.2	Histogram plot of the occupancy of the electronic configurations in system A, B and C taken every fs. Each cluster represents a different classification of the electronic configuration as shown in Figure 5.1.	84

5.3	(Top) Single CI (SCI) energies for simulation A and B for the first 200 fs following excitation to the lowest SCI state. (Bottom) Histogram distributions of the 5 lowest excitation energy levels over a 200 ps simulation. Throughout the simulation, the lowest lying state (in blue) remained populated and varied in character from excitonic to charge-separated.	86
5.4	These plots show the active IR active modes that contribute to the modulation in the CI energies of the systems. Three distinct regions are visible in each plot. The low frequency torsional modes occur between 200 and 500 cm^{-1} , the C=C stretching modes occur between 1300 and 1800 cm^{-1} and the C-H stretching modes occur between 2800 and 3300 cm^{-1}	88

List of Tables

2.1	Experimental parameters used in the Morse potential function Equation 2.13. $E(CH)$ is the energy of the C-H bond at 25 °C , $E_e^{C=C}$ is the equilibrium energy for the C=C bonds, R_e is the equilibrium C=C distance, k_e is the equilibrium force constant, and a is the PPP constant.	28
4.1	Estimated interstate transition rates from Equation 4.20 and vibronic couplings.	71
5.1	Estimated interstate transition rates and vibronic couplings for simulation A, B and C.	89

Chapter 1

Introduction

1.1 General Introduction

Conjugated polymers, shown in Figure 1.1 form a class of molecules that have been studied extensively for over the last three decades. Even in the late 1970's these polymers showed promising potential for possible applications in future electronics. In 1977, Shirakawa, MacDiarmid, and Heeger [1] discovered that films of polyacetylene, the simplest example of a conjugated polymer, become highly conductive after exposure to iodine vapor, work that latter won the team the Nobel Prize in chemistry in 2000. The discovery of the light harvesting properties of Poly(p-phenylenevinylene) (PPV) by Sariciftci [2] in 1993 spurred research into the optoelectronic properties of conjugated polymers. Conducting polymers are generally lighter in weight, more flexible, and less expensive to synthesize and fabricate than their inorganic counterparts which are typically based upon silicon. The mechanical and

material properties of these polymers can be tuned by modifications to the chemical structures, while preserving the desirable electronic properties of the parent polymer. Efficiencies above 10 % are sufficient to allow a small photovoltaic cell to generate enough power to run small electronics. Ever increasing efficiency has allowed conjugated polymers to reach the point of becoming commercially viable in conductive paints, photovoltaic cellphone cases, and large scale solar farms. The revolution of the full utilization of organic photovoltaics in society is inhibited by the lower power conversion efficiency compared to other types of cells shown in Figure 1.2

1.2 Photovoltaic Cells

Photovoltaic Cells are optoelectronic devices that absorb light and transform it into electricity. The world must balance the ever increasing need for energy with the depletion of conventional energy sources and the pollution of the environment from burning them, making the development of efficient photovoltaic cells a global priority. The Earth is bathed daily in free sunlight, making photovoltaic cells an economically feasible alternative to fossil fuels. The absorption of a photon creates singlet excited states (excitons) in the conjugated polymers, that can migrate through the material until reaching the anode or cathode where they are harvested, generating power.

The power conversion efficiencies of highly optimized organic polymer-based photovoltaic cells exceed 10 % under standard solar illumination [3] with reports of efficiencies as high as 12 % [4]. In 1960 Shockley and Queisser [5] found that the maximum efficiency for a donor/acceptor p-n junction is 30 %. The bulk of the

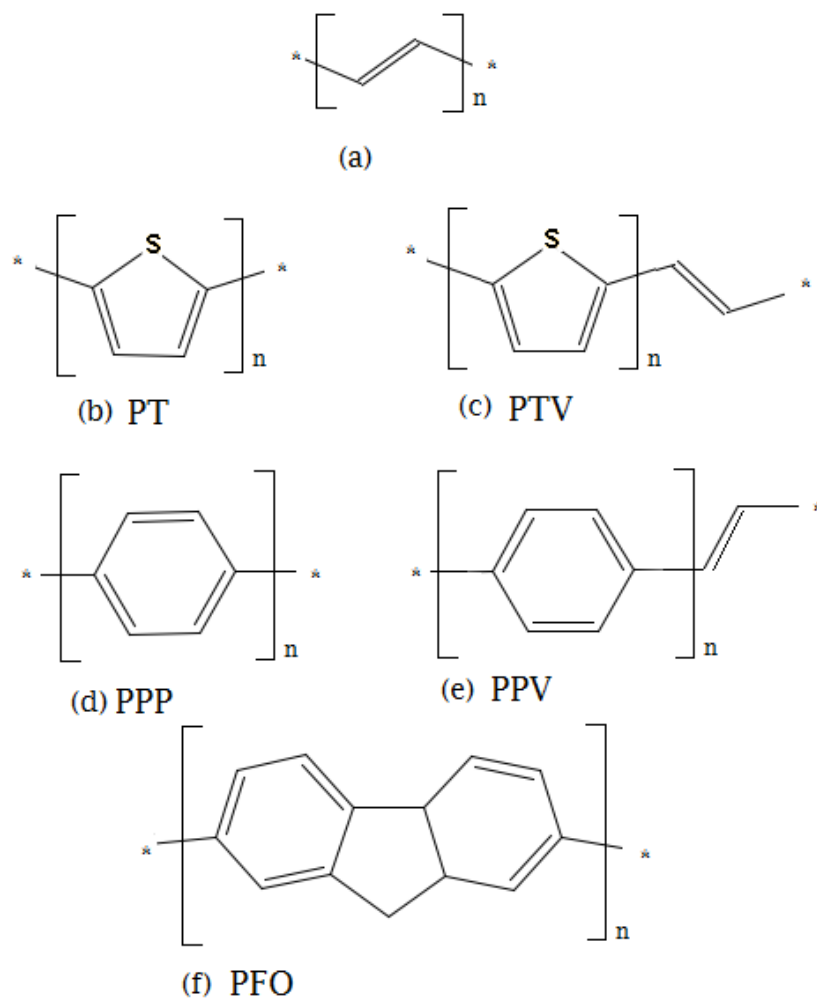


Figure 1.1: Chemical structures of common conjugated polymers: (a) polyacetylene is the simplest conjugated polymer; (b) polythiophene (PT); (c) poly(thienylenevinylene); (d) poly(p-phenylene) (PPP); (e) poly(p-phenylenevinylene) (PPV); and (f) polyfluorene (PFO).

- Multijunction Cells (2-terminal, monolithic)**
- LM = lattice matched
- MM = metamorphic
- IMM = inverted, metamorphic
- ▽ Three-junction (concentrator)
- ▼ Three-junction (non-concentrator)
- ▲ Two-junction (concentrator)
- ▲ Two-junction (non-concentrator)
- Four-junction or more (concentrator)
- Four-junction or more (non-concentrator)
- Single-Junction GaAs**
- ▲ Single crystal
- ▲ Concentrator
- ▽ Thin-film crystal
- Crystalline Si Cells**
- Single crystal (concentrator)
- Single crystal (non-concentrator)
- Multicrystalline
- Silicon heterostructures (HIT)
- ▽ Thin-film crystal
- Thin-Film Technologies**
- CIGS (concentrator)
- CIGS
- CdTe
- Amorphous Si:H (stabilized)
- Emerging PV**
- Dye-sensitized cells
- Perovskite cells (not stabilized)
- Organic cells (various types)
- ▲ Organic tandem cells
- ◆ Inorganic cells (CZTSSe)
- ◇ Quantum dot cells

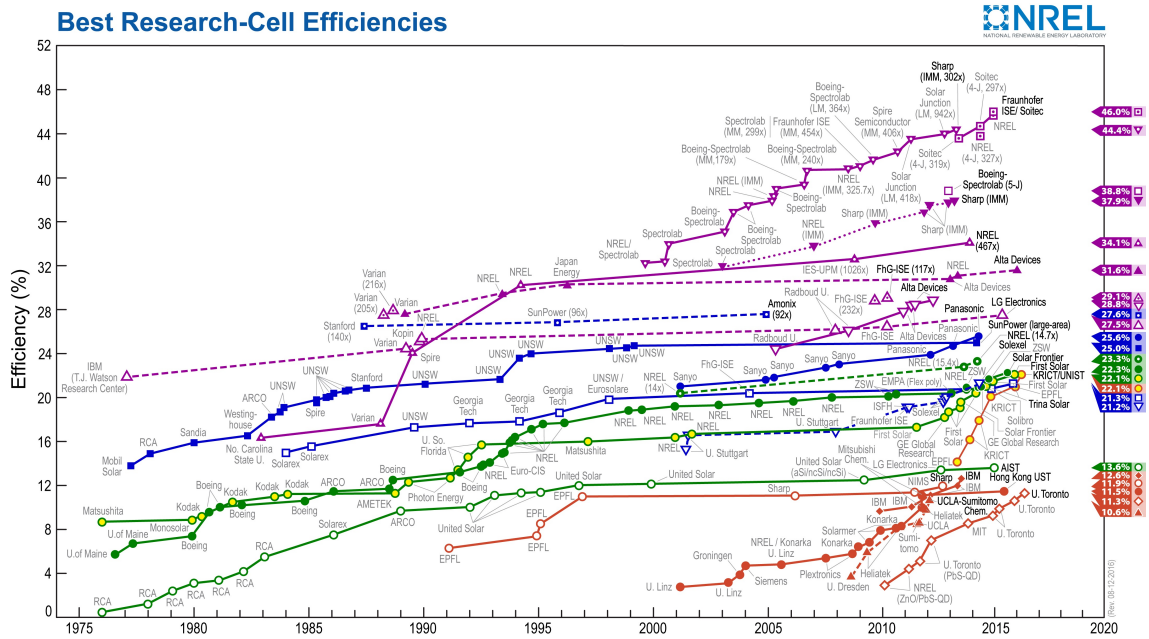


Figure 1.2: The National Renewable Energy Laboratory maintains this plot of the highest confirmed conversion efficiencies for research cells, from 1976 to the present, for a range of photovoltaic technologies. The different colors represent different families of semiconductors, with the red representing organic photovoltaic cells. The most recent world record for each technology is highlighted along the right edge in a colored flag that contains the efficiency and symbol of the technology. This plot is courtesy of the National Renewable Energy Laboratory, Golden, CO. [4]

loss in efficiency occurs as the probability of a photon from a blackbody radiator, interacting with the surface to produce an electron/hole pair is small. Organic photovoltaic materials absorb sun light in a narrow band, from near IR to the blue spectrum, with the bulk of the photons passing through the sample, energetically unable to excite the photovoltaic material. This immediately sets an upper bound to the maximum efficiency of a cell relying on solar radiation. The band gap is another limiting factor for maximum cell efficiency. If the band gap is large it becomes difficult to promote an electron to the excited state and fewer electron/hole pairs are created, however if the band gap is small the electron/hole pairs possess little energy and are prone to recombination. The steady increase in power conversion efficiency indicates that mobile charge carriers can be efficiently generated and collected in well-optimized devices; however, the underlying photo-physical mechanism for converting highly-bound molecular (Frenkel) excitons into mobile and asymptotically free photocarriers remains elusive in spite of vigorous, multidisciplinary research activity. [6, 7, 8, 9, 10, 11, 12, 13, 14, 15, 16, 17, 18]

The generic photophysical pathways that underlie the generation of mobile charge carriers in organic photovoltaic solar cells are sketched in Figure 1.3, the energy level diagram for this process is shown in Figure 1.4. The absorption of a photon by the material produces a π to π^* excitation (exciton) within the bulk (a) that can migrate and diffuse via Forster energy transfer processes. Once in close proximity to a bulk-heterojunction interface, energetic off-sets between the respective HOMO and LUMO levels of adjacent donor and acceptor molecules provide the necessary driving force to separate an exciton into a localized charge transfer (CT) state (b) which typically lies

in the range of 0.25 to 0.4 eV lower in energy. Alternatively, an exciton may dissociate directly via tunneling into charge-separated (CS) or polaron states (c) which may subsequently evolve to contribute to the photocurrent or undergo geminate or non-geminate recombination to form CT states (d). We distinguish CT states from CS states by whether or not the donor and acceptor species are in direct contact (CT) or separated by one or more intermediate molecules (CS). While the current power conversion efficiencies in organic-based devices have just started to reach the level needed for commercialization, the promise of cheaper production cost and wider applicability than their inorganic peers continue to provide sufficient motivation for future development.

1.3 Bulk Heterojunction

A bulk heterojunction is where two conjugated polymers with different electron affinities are combined, one of which acts as an electron donor and transports the holes, while the other acts as an electron acceptor and transport material. There are two basic types of heterojunctions, bi-layer and blended. The bi-layer heterojunctions are made by adjoining the donor and acceptor phases, forming a single small interface. The ability of the heterojunction to form free charge carriers depends on two fundamental characteristics, the mobility of the charge carriers and the life time of the excitons. A good photovoltaic cell must have high mobility and long emission lifetimes, along with the ability to absorb photons over a large spectrum. Excitons must migrate from the bulk to the interface and separate, next migrating away from

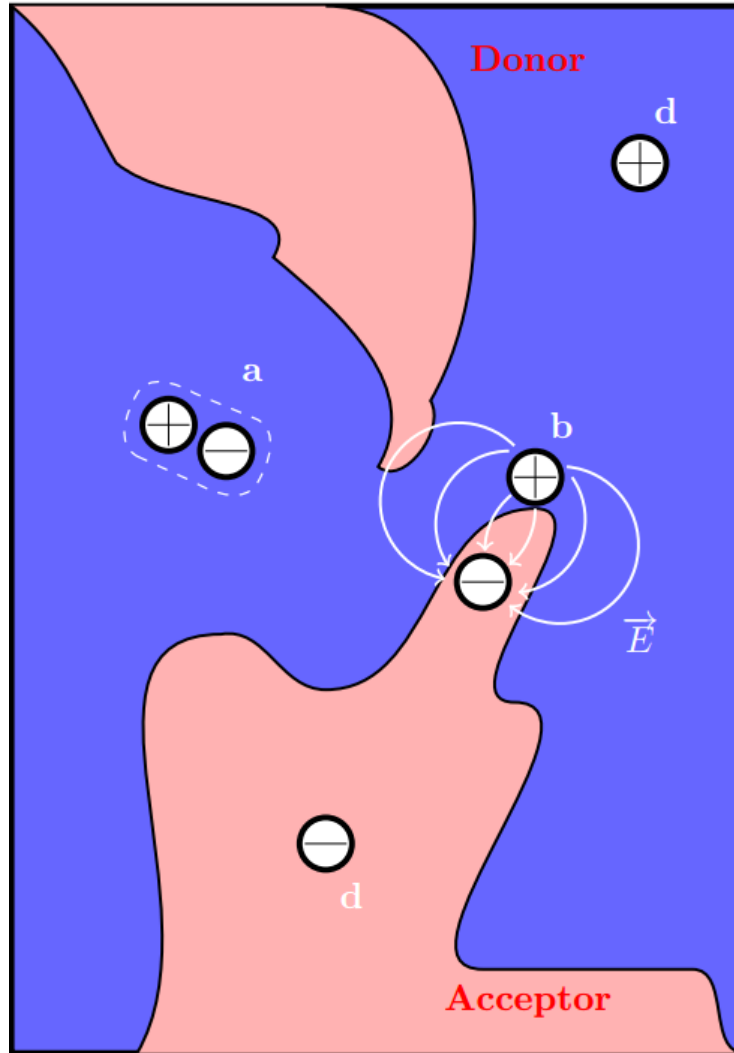


Figure 1.3: Schematic diagram of a bulk heterojunction. The red represents the donor regions while the blue represents the acceptor regions. They are blended thereby increasing the interfacial surface area and the probability of exciton formation in the vicinity of the interface. The charges still require a pathway to the electrodes leading to greater sensitivity to the interfacial morphology. The exciton formed inside the bulk shown by the electron/hole pair (1), migrates to the interface where it will separate. The resulting charge transfer state (2), must overcome the Coulomb attraction and migrate away from the interface (3).

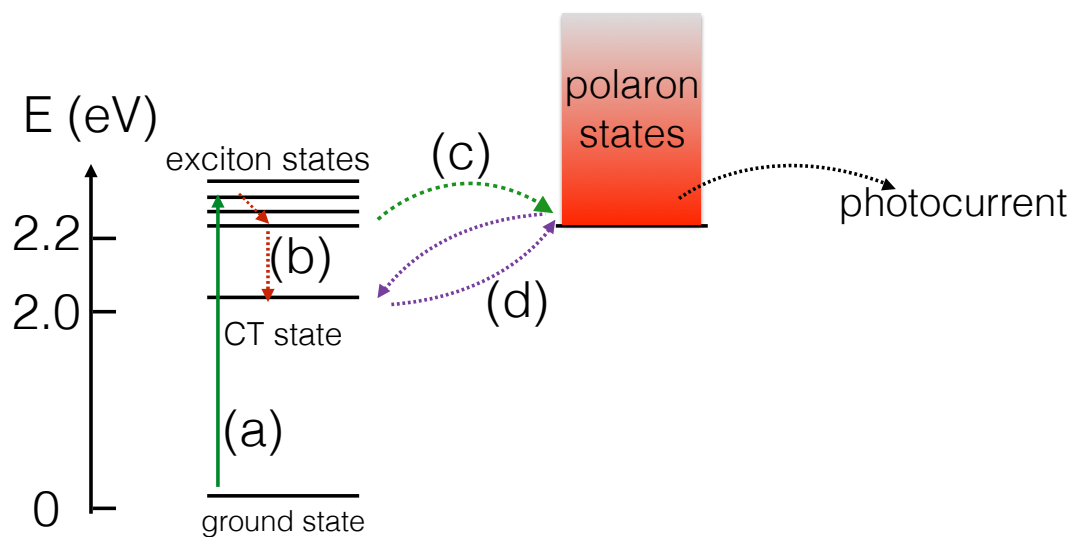


Figure 1.4: Jablonski diagram showing relative energetic positions of excited states in a bulk-heterojunction system. The discrete states on the left are assumed to be localized excitons or charge-transfer states while the polaron states are assumed to be a quasi-continuum of mobile charge-separated states within the bulk. The latter of these are presumed to be responsible for producing photocurrent from a given device.

the interface to the probes, generating power. In by-layer heterojunctions only excitons formed near the interface have a lifetime long enough to form charge transfer states, therefore only a limited fraction of the excitons produced will actually dissociate. The blended bulk heterojunction is where the donor and acceptor phases are mixed, increasing the contact between the donor/acceptor molecules, allowing the formation of a larger interface as seen in Figure 1.3. This increases the probability that an exciton will be formed close enough to the interface to have a chance of separating. The increase in charge transfer states produced by the enlarged interface has the potential to substantially improve the cells performance. However, to benefit from the increase in exciton formation near the interface the charge transport through the bulk regions inside the heterojunction must also be efficient. The random morphology of blended heterojunctions inhibit the ability of the charge carriers to find a linear, contiguous path to the collector electrodes. Instead, a percolated path becomes necessary, further increasing charge recombination as compared to the bi-layer heterojunction. For these reasons, the performance of blended bulk heterojunctions is critically dependent on the nano-morphology of the interface and bulk regions.

The nano-morphology, especially around the interface of blended heterojunctions is still a hotly debated topic of research. Qualitatively the effects of the morphology and especially the size of the PCBM clusters in the bulk is rather well-understood. Too large of a PCBM cluster quenches efficiency by reducing the ability of the hole to migrate to the interface and excitons created deep within large clusters may not dissociate. The quantitative understanding of the influence of the PCBM content and

PCBM cluster size is still under debate. It was shown by Duren *et al.* [19] that the highest efficiency of a MDMO-PPV/PCBM blend occurred when the weight percent of PCBM increased over 80 %. This result is interesting as PCBM hardly absorbs sun light. It was found that for weight fractions below 80 % the transport of holes along with the efficiency of separation provide the limiting factors for cell performance. [20] This result leaves the impression that hole transport, which presumably takes place via the conjugated donor polymer is enhanced by the high weight percent of PCBM. The question of whether a ordered network of PCBM molecules and aggregates is necessary for effective electron transport however, remains unanswered. [21, 22, 23]

The electronic properties of donor/acceptor organic conjugated polymers arise from the delocalized π -system of electrons. The π -system is primarily an intramolecular network of orbitals extending along the backbone of the polymer chains. This is precisely the case in unsaturated organic systems where the π -conjugated electronic states extend over at least a couple of molecular units. The highest occupied molecular orbitals (HOMOs) and the lowest unoccupied molecular orbitals (LUMOs) give rise to a conduction and valence band, separated by the band gap. For linear polymers like PPV the valence and conduction bands for the π to π^* transition are typically between 1-3 eV and the electronic states of the system are extended over significant length scales such that electrons can move quite freely along the backbone of the polymer chains. This allows intrachain charge transport to be very efficient, however, defects in the chains due to torsions, chemical impurities, and so on limit the length of the π -orbitals to the extent that one can consider many large conjugated polymer molecules to be linked sequences of smaller interacting conjugated regions.

Interchain charge transport is typically the limiting factor for charge mobility inside the polymer systems.

An exciton is often characterized as an electron/hole pair bound by Coulomb attraction, however, the exciton is electrically neutral and able to move by diffusion. For this reason two different materials with different electron affinities are combined to form the interface, the difference in electron affinities act as a driving force for charge separation. The charges are generated by the dissociation of the electron and hole at the interface into a charge-transfer state, however, charge mobility is greatly hampered by the Coulomb attraction between the charges at the interface. The charge-transfer states must break the Coulomb attraction and migrate away from the interface to form free charges that can be harvested by the probes. The dielectric constant of conjugated organic polymers are relatively low (≈ 3), dramatically reducing the screening between the electron/hole pair. The barrier for separation of the charges is low enough at 300 K that thermal fluctuations will be sufficient to allow efficient electron/hole separation at some radius r_c .

$$kT = \frac{e^2}{\epsilon r_c} \quad (1.1)$$

Using Equation 1.1, the radius for separation is approximately 20 nm, which is on the order of a few molecular units.

Ultrafast spectroscopic measurements on organic photovoltaic systems have reported that charge photoexcitations are generated on ≤ 100 -fs [11, 16, 24, 25, 26, 27, 28] timescales; however, full charge separation to produce free photocarriers is expected to be energetically expensive given the strong coulombic attraction between

electrons and holes due to the low dielectric constant in molecular semiconductors. Nonetheless, experiments by Gelinas *et al.*, in which Stark-effect signatures in transient absorption spectra were analysed to probe the local electric field as charge separation proceeds, indicate that electrons and holes separate by as much as 40 Å over the first 100 fs and evolve further on pico-second time scales to produce unbound and hence freely mobile charge pairs. [10] Concurrently, transient resonance-Raman measurements by Provencher *et al.* demonstrated clear polaronic vibrational signatures on sub-100 fs on the polymer backbone, with very limited molecular reorganization or vibrational relaxation following the ultrafast step. [15] Such rapid through-space charge transfer between excitons on the polymer backbone and acceptors across the heterojunction would be difficult to rationalize within Marcus theory using a localized basis without invoking the unphysical distance dependence of tunneling rate constants [29] and appear to be a common feature of organic polymer bulk heterojunction systems.

1.4 History of Computational Methods Employed to Study Conjugated Polymers

The discovery of the structure of benzene in 1865, with its alternating single and double bonds, along with its tendency to react through the ortho, meta, and para positions puzzled generations of scientists. In 1926, Erwin Schrödinger published his

famous Schrödinger equation

$$H|\Phi\rangle = E|\Phi\rangle \quad (1.2)$$

Where the Hamiltonian of the system is given by

$$H = -\sum_{i=1}^N \frac{1}{2} \nabla_i^2 - \sum_{A=1}^M \frac{1}{2M_A} \nabla_A^2 - \sum_{i=1}^N \sum_{A=1}^M \frac{Z_A}{r_{iA}} + \sum_{i=1}^N \sum_{j>i}^N \frac{1}{r_{ij}} + \sum_{A=1}^M \sum_{B>A}^M \frac{Z_A Z_B}{R_{AB}} \quad (1.3)$$

The first term in Equation 1.3 is the operator for the kinetic energy of the electrons; the second term is the operator for the kinetic energy of the nuclei; the third term represents the coulomb attraction between the electrons and the nuclei; the fourth term represents the repulsion between electrons and the fifth term represents the repulsion of the nuclei. This approach answered many questions of the time and revolutionized the way chemists and physicists look at atoms and molecules. However, this Hamiltonian is far too complex for anything larger than the smallest molecular dimers and must be simplified to suit even small conjugated organic systems such as benzene. In 1930, Erich Hückel presented the Hückel theory [30], a simple method for calculating the orbital energies of conjugated organic molecules based upon the symmetry of the molecule.

1.4.1 Hückel Theory

The Hückel theory assumes that conjugated systems form a chain of unsaturated alternating single and double bonds. In these systems the C atoms that make the backbone of the polymers are sp_2 hybridized, forming 3 σ bonds with neighboring

atoms. The remaining $2p_z$ orbital is perpendicular to the σ -plane and forms overlapping π bonds, delocalizing these electrons across the entire polymer backbone. This delocalization decreases the overall kinetic energy of the electrons and lowers the total electronic energy of the system. So the Hückel model assumes that there is an energy, α associated with placing an electron into a $2p_z$ orbital as well as an energy, β associated with moving the electron to a neighboring $2p_z$ orbital.

$$\langle \phi_i | H | \phi_j \rangle = \beta \quad (1.4)$$

$$\langle \phi_i | H | \phi_i \rangle = \alpha \quad (1.5)$$

The overlap integrals between non-neighboring orbitals are assumed to be zero, $\langle \phi_i | \phi_j \rangle = \delta_{ij}$. This provides a sufficient basis to expand the electronic wave function as

$$|\Psi\rangle = \sum_{j=1}^N c_j |\phi_j\rangle \quad (1.6)$$

The Coulombic interaction between the electrons is also neglected so the energy eigenvalues are found by the one-electron Schrödinger equation.

1.4.2 Example of Hückel Model on (1,3)-butadiene

A (1,3)-Butadiene molecule is one of the simplest conjugated systems we can study. Applying the Hückel model to (1,3)-butadiene generates the adjacency matrix

$$H = \begin{pmatrix} \alpha & \beta & 0 & 0 \\ \beta & \alpha & \beta & 0 \\ 0 & \beta & \alpha & \beta \\ 0 & 0 & \beta & \alpha \end{pmatrix}$$

Taking the determinant of the adjacency matrix, yields the eigenvalues and eigenvectors of the system.

$$\begin{vmatrix} x & 1 & 0 & 0 \\ 1 & x & 1 & 0 \\ 0 & 1 & x & 1 \\ 0 & 0 & 1 & x \end{vmatrix} = 0$$

In the equation above the α and β terms have been combined into the diagonal elements, $x = (\alpha - E)/\beta$. Expanding the determinant gives $x^4 - 3x^2 + 1 = 0$. The fourth order polynomial has four roots that correspond to the orbital energies of (1,3)-butadiene as shown in Figure 1.5.

1.5 The MM/QM Approach

In 1976, Warshel et al. [31] published a methodology that blended the simplicity and speed of classical mechanics (MM) with the ability to treat part of the molecule using quantum mechanics (QM). This method is referred to as a MM/QM approach. Warshel started by implementing a Born-Oppenheimer approximation

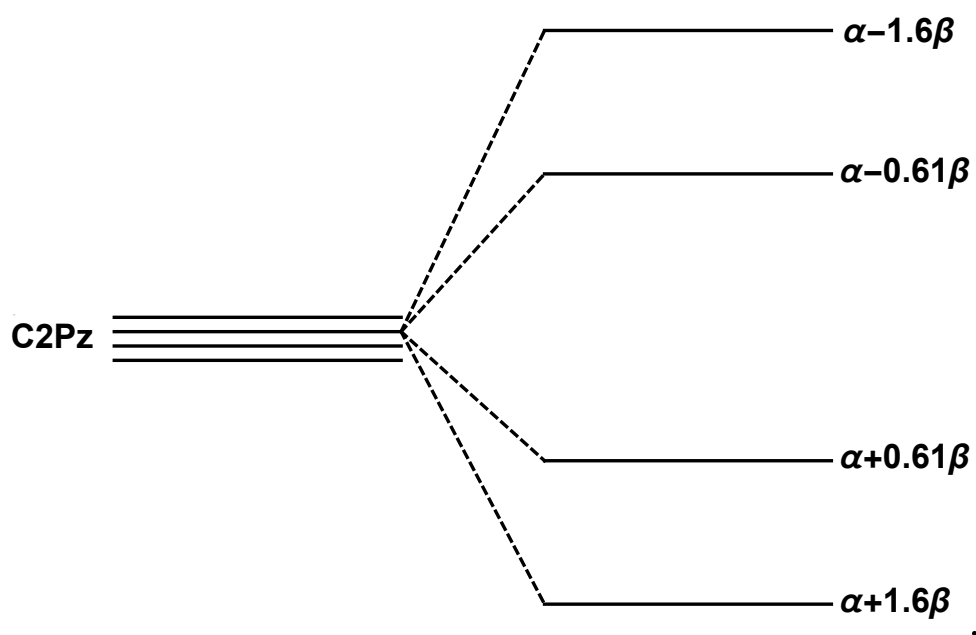


Figure 1.5: The energy levels and orbitals for (1,3)-butadiene, generated using the Hückel model. The energies are found by solving the roots of the fourth order polynomial generated by taking the determinant of the adjacency matrix.

decoupling the nuclear and electronic portions of the wave-function. This approximation states that the mass of the nuclei are so much greater than the mass of the electrons, assuming that the nuclei do not react fast enough to the change in electron density and can be treated as stationary, essentially allowing electrons to move in a field of fixed nuclei. The energy of the system is decomposed into three portions, the classical, the quantum, and a coupling term between the classical and quantum terms. The quantum potential energy is obtained using the QCFF/ALL semi-empirical method. [32] This method carves the valence electrons from the chosen regions and uses hybrid atomic orbitals to form an overlap between the adjacent non-interacting regions. Configuration Interaction Double excitation corrections are used as a first correction to the ground state. A modified intermediate neglect of differential overlap is employed, where the attraction $\langle u | V_B | u \rangle$ between an electron in atomic orbital ϕ_u of atom A, and the core of atom B, are given by

$$\langle u | V_B | u \rangle = -C_B \gamma_{AB} \quad (1.7)$$

where C_B is the core charge of the valence shell on atom B. The two-center repulsion integrals γ_{AB} are calculated by the Ohno-Klopman expression [33],

$$\begin{aligned} \gamma_{AB} &\rightarrow \frac{1}{2}(F_A^0 + F_B^0) & \text{as } R_{AB} \rightarrow 0 \\ \gamma_{AB} &\rightarrow \frac{e^2}{R_{AB}} & \text{as } R_{AB} \rightarrow \infty \end{aligned} \quad (1.8)$$

where the average one-center Coulomb repulsion integral is F^0 . With these approximations, the elements of the core matrix H and the Hartree-Fock matrix F for a

closed shell system are

$$H_{uu}^{AA} = U_{uu} - \sum_{B \neq A} C_B \gamma_{AB} \quad (1.9)$$

$$H_{uv}^{AA} = 0$$

$$H_{uv}^{AB} = \beta_{uv}^C \quad (1.10)$$

$$F_{uu}^{AA} = U_{uu} + \frac{1}{2}q_u(uu, uu) + \sum_{v \neq u}^A q_v((uu, uv) - \frac{1}{2}(uv, uv)) + \sum_{B \neq A} (Q_B - C_B)\gamma_{AB} \quad (1.11)$$

$$F_{uv}^{AA} = P_{uv} \left(\frac{2}{3}(uv, uv) - \frac{1}{2}(uu, uv) \right) \quad (1.12)$$

$$F_{uv}^{AB} = \beta_{uv}^C - \frac{1}{2}P_{uv}\gamma_{AB} \quad (1.13)$$

Here q refers to the electron densities of the atomic orbitals, Q is the total valence shell electron density for an atom, and P represents the bond order matrix. The total molecular energy can be written as

$$E = \frac{1}{2} \sum_u \sum_v P_{uv} (H_{uv} + F_{uv}) + \sum_{A < B} C_A C_B \gamma_{AB} \quad (1.14)$$

For developing this methodology to study enzymatic processes in large protein structures, Warshel received the Nobel prize in chemistry in 2013.

1.6 Dissertation Overview

In this dissertation, we are interested in describing the properties of electron/hole separation at model PPV/PCBM heterojunctions. We developed a MM/QM model that allows the quantum mechanical treatment of the π electrons on multiple conjugated polymers. The π systems are in constant contact with the local environment, all of the molecular forces are described using the MM3 parameter set. This allows for a more realistic picture of the excited state dynamics that occur around the interface, reflecting the long term fates of the excited states. The process and timescales by which electron and hole separation occur are of paramount interest, however, *ab-initio* methods cannot currently simulate large enough clusters of molecules to derive a comprehensive picture of the interface. In this dissertation, we introduce an emerging picture of carrier generation in OPV systems in which interfacial electronic states can rapidly decay into charge-separated and current producing states via vibrionic degrees of freedom.

In the subsequent chapters, we will present the result of our theoretical investigations on PPV/PCBM heterojunction systems. Chapter 2 explores the methodology employed to study polymer heterojunctions. We introduce the Pariser-Parr-Pople and Configuration Interaction Singles methodology used in the π -MDX code, a unique molecular mechanics(MM)/Quantum mechanics(QM) package developed by the Bitter group to simulate large systems of blended PPV/PCBM molecules. In chapter 3, we introduce our simulation methods. A π -MDX handbook for future reference is introduced and a brief introduction to the creation of simulation

cells is given. In chapter 4, we investigate the role of structural fluctuations and environmental noise in the electron/hole separation kinetics of a single PPV/PCBM heterojunction. We use the simple model of a two level system coupled to the environment to describe the behavior of the excited states of the blended heterojunction. The time evaluation of the density matrix is used to derive rate constants between excited states for the PPV/PCBM heterojunction. In chapter 5, we investigate the effect local packing has on the delocalization of charges at a model donor/acceptor interface. We use the same methodology outlined in chapter 4 only applied to three different PPV/PCBM systems.

Chapter 2

Methods

2.1 Introduction

Understanding the charge separation dynamics of excitons in blended bulk heterojunctions constitutes one of the fundamental problems in describing the behavior of photovoltaic cells. Various spectroscopic methods have provided many details about the mechanisms of charge generation but a complete and general understanding of these reactions has yet to be achieved. The exact role of important topics such as blend ratio [19, 34, 35, 36, 37, 38], electron separation dynamics [40, 41, 42, 43, 44, 45], and even the role disorder at the interface plays in electron/hole separation remains unclear. [21, 23, 46, 47, 48, 49] The relative importance of all the factors involved in charge separation require a proper theoretical method that can be used together with the available experimental information to form a cohesive picture of the processes driving charge separation in bulk heterojunctions.

The conformation of the solvent and polymer chains can be adequately simulated using empirical energy functions based on the classical contributions of bond stretching, bond angle bending, bond twisting, and non-bonded interactions. While the mechanism and energetics of the exciton separation process can only be studied using a quantum mechanical approach. Previous quantum mechanical calculations on bulk heterojunctions have been limited in several respects. Primarily, most simulations deal with an over-simplified model system, consisting of only one or two molecules representing the interactions of the entire heterojunction interface. Another issue is that most quantum mechanical techniques treat the system as if it were in a vacuum, neglecting the effect of solvent and the dielectric constant on the system. This is a common approximation, made by a simple Hückel treatment and *ab-initio* calculations, however, there must be a way where the relevant quantum portion of the calculation can be extended over a large enough area to better simulate an interface while allowing the system to interact with its environment.

We are interested primarily in the π to π^* transition of conjugated polymers at the interface. Because the quantum mechanical treatment of the whole donor/acceptor interface is computationally impossible, it becomes necessary to simplify the problem and use a hybrid MM/QM approach. Where a cluster of molecules around the interface have the π -system treated quantum mechanically while all of the other molecules and the backbones of the system are treated classically. This approximation is convenient as the σ electrons of the system are considered inert. This type of approach combines the ease and low computational cost of classical mechanics with the more rigorous quantum approach needed to understand charge separation. This is not an

easy methodology to implement, the separation of the π and σ systems are rarely applied to more than a single molecule, leaving many unknowns in how to correctly implement such an approximation into simulating large collections of molecules.

2.2 Pariser-Parr-Pople Hamiltonian

In the early days of quantum chemistry, computers were huge and slow, scientists had to rely on pen and paper to find analytical solutions to problems. The inability to numerically solve complex systems severely limited the scope of the calculations performed. To accommodate this problem, special restrictions were developed allowing computation of the outermost valence electrons, while packing the effect of the core electrons into the nuclear terms. The conjugated backbone of a molecule is held together by a σ bonding network, these bonds are considerably stronger than the π bonds and keep the molecule intact, even following photoexcitation. The π electrons have substantially higher orbital energies as well and are separated energetically from the σ electrons, allowing the π and σ systems to be assumed as non-interacting. So if we can consider the electronic dynamics as taking place within the π system and treat the localized σ bonds as skeletal framework, the computational time required to tackle the electronic portion of the Hamiltonian can be greatly reduced.

Here we discuss the implementation of the PPP model into the Tinker [50] MM/QM package. The π -MDX code has been developed by the Bittner group to simulate the excited-state dynamics of large systems of conjugated polymers around

the interface. The approach assumes the π -electronic system is decoupled and orthogonal to the σ -bonding system and that each C atom in the π -system contributes one C $2p_z$ orbital. We denote the local (atomic orbital) basis as ϕ_u for an orbital on atom u and molecular orbital wave function as

$$\Psi_i = \sum_{u=1}^k C_{ui} \phi_u \quad (2.1)$$

The Ψ_i are single particle solutions of the Hartree-Fock equation such that

$$\sum_v F_{uv} C_{vi} = E_i \sum_v S_{uv} C_{vi} \quad (2.2)$$

where $S_{uv} = (\phi_u | \phi_v)$ is the overlap integral between orbitals u and v and F_{uv} is the Fock operator defined as

$$F_{uv} = H_{uv}^{core} + \sum_a \sum_{\lambda\sigma}^{N/2} C_{\lambda a} C_{\sigma a}^* [2(uv | \sigma\lambda) - (u\lambda | \sigma v)] \quad (2.3)$$

for a closed shell ground state with N-electrons. The bond-charge density matrix, P , can be found by

$$\begin{aligned} &= 2 \sum_a \sum_{\lambda}^{N/2} C_{\lambda a}^* \phi_{\lambda}^*(r) \sum_{\sigma} C_{\sigma a} \phi_{\sigma}(r) \\ &= \sum_{\lambda\sigma} 2 \sum_a^{N/2} C_{\lambda a} C_{\sigma a}^* \phi_{\lambda}(r) \phi_{\sigma}^*(r) \\ &P_{\lambda\sigma} = 2 \sum_a^{N/2} C_{\lambda a} C_{\sigma a}^* \end{aligned} \quad (2.4)$$

where λ and σ represent $2p_z$ orbitals. The bond-charge density matrix is a probability matrix, represented by the spatial wave function $\Psi_i(\mathbf{r})$, then the probability of finding that electron in a volume element, dr , at a point r is $|\Psi_i(r)|^2 dr$. The probability of finding an electron in dr at r is also given by

$$\rho(r) = 2 \sum_i^{N/2} \Psi_i^*(r) \Psi_i(r)$$

where Ψ_i is an occupied molecular orbital. Using the molecular orbitals expansion of Equation 2.1 we generate the bond-charge matrix $P_{\lambda\sigma}$ as shown by Equation 2.4. Plugging $P_{\lambda\sigma}$ into Equation 2.3

$$= H_{uv}^{core} + \sum_{\lambda\sigma} P_{\lambda\sigma} [(uv | \sigma\lambda) - \frac{1}{2}(u\lambda | \sigma v)] \quad (2.5)$$

Where

$$(uv | \sigma\lambda) = \int \int dr_1 dr_2 \phi_u^*(1) \phi_v(1) \frac{1}{r_{12}} \phi_\sigma^*(2) \phi_\lambda(2) \quad (2.6)$$

and we have defined a core-Hamiltonian matrix

$$H_{uv}^{core} = \int dr_1 \phi_u^*(1) h(1) \phi_v(1) \quad (2.7)$$

the one-electron operator $h(1)$ describes the kinetic energy and nuclear attraction of an electron to the nuclei.

These equations are meant to be applied to all electrons in a molecule, including the inner shell σ electrons. In the π -MDX code, we assume that the effect of the σ

electrons on the π system can be included within the H_{uv}^{core} matrix elements. This is achieved by calculating the effective charge on the rigid cores as if the σ electrons were shielding them. The next assumption is that the overlap integral, S_{uv} , is neglected unless $u = v$, where it is 1.

$$[\phi_u(1)\phi_v(1)] = \delta_{uv}\phi_i^2(1) \quad (2.8)$$

In the π -MDX code, all two-electron integrals which depend on the overlapping of charge distribution of different orbitals are neglected. This means that the Coulomb repulsion $(uv | \sigma\lambda)$ is neglected unless $u = \sigma$ and $v = \lambda$. The Complete Neglect of Differential Overlap (CNDO) approximation greatly increases the speed of the calculation by reducing the number of two-electron integrals from $\approx N^4$ in *ab-initio* calculations to $\approx N^2$. The new Fock matrix and Hamiltonian can be written as

$$F_{uu} = H_{uu}^{core} + \frac{1}{2}P_{uu}(uu | uu) + \sum_{\sigma \neq u} P_{\sigma\sigma}(u\sigma | \sigma u) \quad (2.9)$$

$$F_{uv} = H_{uv}^{core} - \frac{1}{2}P_{uv}(uv | uv) \quad (u \neq v) \quad (2.10)$$

The H_{uu}^{core} terms are the diagonal matrix elements for the one electron Hamiltonian contain the kinetic energy and interactions with all distant cores. The H_{uv}^{core} off diagonal terms are the couplings between nearest neighbors, representing the fact that electrons can move by virtue of being in the field of two σ cores. In the π -MDX

code the H^{core} terms are calculated using a semi-empirical method. The H^{core} matrix generated is used as an approximation for the initial guess at the Fock matrix in the SCF procedure. The diagonal H_{uu}^{core} terms are given by the equation

$$H_{uu}^{core} = \sum_u ip(u) + (1 - q(u)rp(u)) \sum_{u \neq v} -q(v)\gamma(u, v) \quad (2.11)$$

where $ip(u)$ is the ionization potential of nuclei u found in the MM3 parameter file, $q(u)$ represents the π electron contribution from nuclei u , $rp(u)$ is the repulsion integral value for atom u , and $\gamma(u, v)$ is the repulsion integral between nuclei u and v . The off diagonal terms of the H_{uv}^{core} matrix are calculated using the Whitehead and Lo formula [51, 52], where all the input parameters are based on experimental observables. The bond energy $E_b^{(C=C)}$ of a C=C bond is partitioned into π and σ bond energies.

$$E_b^{(C=C)}(R_{i,j}) = E_{\pi b}(R_{i,j}) + E_{\sigma b}(R_{i,j}) \quad (2.12)$$

The equilibrium C=C bond energies for ethylene and benzene are determined by experiment, while the distance dependence of the C=C bond can be expressed by a Morse potential function.

$$E_b^{C=C}(R_{i,j}) = E_e^{C=C} [2e^{-a(R_{i,j}-R_e)} - e^{-2a(R_{i,j}-R_e)}] \quad (2.13)$$

The force constants and equilibrium bond lengths are taken as experimental values from Lo *et al.* [51] and shown in Table 2.1.

Table 2.1: Experimental parameters used in the Morse potential function Equation 2.13. $E(CH)$ is the energy of the C-H bond at 25 °C, $E_e^{C=C}$ is the equilibrium energy for the C=C bonds, R_e is the equilibrium C=C distance, k_e is the equilibrium force constant, and a is the PPP constant.

	$E(CH)$ (kcal/mole)	$E_e^{C=C}$ (kcal/mole)	R_e (Å)	k_e (dyn/cm)	a (Å ⁻¹)
Ethylene	102.13	129.172	1.334	9.57×10^5	2.309
Benzene	102.13	117.558	1.397	7.50×10^5	2.142

From Equations 2.9 and 2.10 the π -bond energy can be determined, assuming $P_{i,j}$.

$$E_{\pi b}^{ethylene} = -\left[\frac{1}{2}g11 + 2H_{uv} - \frac{1}{2}g12\right] \quad (2.14)$$

$$E_{\pi b}^{benzene} = -\left[\frac{1}{4}g11 + \frac{4}{3}H_{u,v} - \frac{2}{9}g12 - \frac{1}{36}g14\right] \quad (2.15)$$

Substituting Equation 2.14 and 2.13 into Equation 2.12 for ethylene, and Equation 2.15 and 2.13 for benzene, the expression $H_{u,v}$ for the resonance integral can be determined by

$$H_{u,v} = \frac{3}{2}\left[E_b^{C=C}(R_{u,v})_{benz} - (E_b^{C=C}(R_{u,v})_{ethy} - \frac{1}{4}g11 + \frac{5}{18}g12 - \frac{1}{36}g14)\right] \quad (2.16)$$

Where g11, g12, and g14 are the one-center, two-center, and long-range Coulomb interactions. This procedure gives the correct functional dependence of H_{uv} on distance for the π -electron system. It also produces the correct σ -bond length of 1.505

\AA for a single C-C bond. The ability of this method to reproduce such intrinsic information of the system demonstrates the accuracy of this approximation when looking at conjugated C=C systems. In the Fock matrix shown in Equation 2.9, $(uu | uu)$ is a one-center Coulomb integral (g11) given by

$$g11 = \int \phi_u^*(1)\phi_u(1)\frac{e^2}{R_{12}}\phi_u^*(2)\phi_u(2)d_1d_2 \quad (2.17)$$

and the two-center Coulomb integral $(u\sigma | \sigma u)$ (g12) is given by

$$g12 = \int \phi_u^*(1)\phi_u(1)\frac{e^2}{R_{12}}\phi_\sigma^*(2)\phi_\sigma(2)d_1d_2 \quad (2.18)$$

The total π -electron energy is given by

$$E_\pi = \sum_{u<v} Z_u Z_v R_{uv}^{-1} + \frac{1}{2} \sum_{uv} P_{uv} (H_{uv} + F_{uv}) \quad (2.19)$$

where the first term represents the effective nuclear interaction between nuclei Z_u and Z_v .

The PPP model shown above implements three major approximations, greatly increasing the speed at which calculations can be performed. The first approximation places the effect of the σ core into the potential term of the H^{core} matrix. Such that the effective nuclear charge in the potential term, now reflects the presence of all the σ -core electrons associated with the nuclei. The second approximation introduced CNDO, where the overlap integral, S_{uv} , will be neglected unless $u = v$, greatly

reducing the number of two electron integrals. The third approximation is that the H^{core} matrix can be calculated using semi-empirical means. It can be noted that by removing all of the terms in Equation 2.9 and 2.10 except for the H^{core} terms you reproduce a Hückel type model where H_{uu} represents the energy associated with occupying an orbital α and H_{uv} represents β the energy associated with moving an electron to a neighboring orbital.

2.3 Configuration Interaction (Singles)

The π to π^* transition that we are interested in modeling requires that we have the ability to construct excited states of conjugated polymers. The HF approximation forms a good approximation to the ground state of the system, however, it does not provide any information about the excited states of the system. The HF procedure produces a set of spatial orbitals, $\psi(r)$, which are composed of (2k) spin orbitals $\chi_{(1)\alpha}$ and $\chi_{(2)\beta}$. The spin orbitals must follow the antisymmetry principle where the ground-state wave-function is given by solving the Slater determinant. The Hartree Fock ground-state wave-function is given by

$$|\Psi_0\rangle = |\chi_1\chi_2\cdots\chi_\alpha\chi_\beta\cdots\chi_N\rangle \quad (2.20)$$

Where a number of different single determinants can be formed from N electrons and $2K$ spin orbitals.

$$\binom{2K}{N} = \frac{(2K!)}{N!(2K-N)!}$$

For a simple molecule such as oxygen the number of determinants is huge.

$$\binom{32}{16} = \frac{(32!)}{16!(16)!} = 601,080,390.$$

So in practice, the number of single determinants must be truncated to a manageable level. This is where we start our discussion of Configuration Interaction Singles (CIS).

In CIS calculations, the HF ground state Equation 2.20 can be considered as a reference state, other possible determinants are classified by how they differ from the reference state. This is achieved by replacing a set χ_a with a new set χ_r as seen in Figure 3.2. The full CI wave function is comprised of all possible excitations in the system

$$|\Phi_0\rangle = C_0 |\Psi_0\rangle + \sum_{ar} C_a^r |\Psi_a^r\rangle + \sum_{r<s} \sum_{a<b} C_{ab}^{rs} |\Psi_{ab}^{rs}\rangle + \sum_{a<b<c} \sum_{r<s<t} C_{abc}^{rst} |\Psi_{abc}^{rst}\rangle + \dots \quad (2.21)$$

where a , b , and c represent occupied orbitals and r , s , and t represent virtual orbitals. In the π -MDX code, two variables that determine how many atomic orbitals are used inside the truncation. The variables for the upper (virtual) and lower (occupied) molecular orbitals are set to 10 orbitals in each, giving a 20 molecular orbital CI subspace. The new determinants can be taken to represent approximate excited states of the system. A singly excited determinant is one where an electron, which

occupied χ_a in the HF ground state is promoted to a virtual-spin orbital, χ_r , as seen in Figure 2.1. For the excited states, the singly excited determinants give the most important contribution and the simplest way to construct the excited state wave function is to take a linear combination of the singly excited determinants. Since they do not interact with the ground state (Brillouin theorem), and consequently there is no danger of falling back to the ground state, the wave function can be optimized using the variational principle. The π -MDX code includes a singlet/triplet switch, that allows formation of either singlet or triplet virtual orbitals. Of the possible 400 singly excited configurations allowed for 20 electrons and 40 spin adapted orbitals, we consider 100 configurations in the formation of the new excited state wave function. The total number of configurations can be reduced by specifying whether the excited state wave function will be a singlet or triplet. This is because the mixing of wave functions with different spins is prohibited. So a singlet wave function is constructed by determinants that contain the same number of α and β spin orbitals. This reduces the number of configurations that span the full CIS-singlet wave function to 200. Digitalization of the CIS matrix takes place over the excited state configurations, yielding energy eigenvalues and corresponding eigenvectors detailing the weight of every singly excited determinant in the excited state. The total wave function for the system is represented by the HF ground state and the correction to the ground state to form the excited-state wave function

$$|\Phi_0\rangle = C_0 |\Psi_0\rangle + \sum_{ar} C_a^r |\Psi_a^r\rangle \quad (2.22)$$

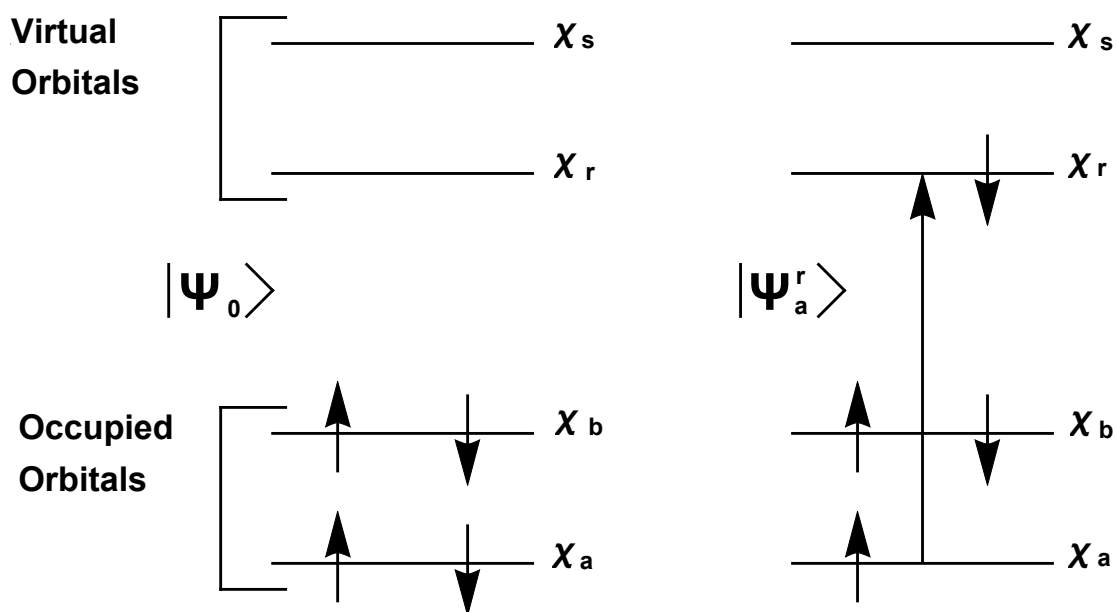


Figure 2.1: The Hartree-Fock ground state $|\Psi_0\rangle$ and Configuration Interaction Singlet excited state determinants $|\Psi_a^r\rangle$.

It is important to note that in the π -MDX code, we use a super-system of MO's. Each molecule inside the π -active system contributes one π electron and hence a $2p_z$ orbital to the total system. The molecular orbitals, formed from the atomic orbitals are ranked by their energies into a single super-system list of molecular orbitals and filled accordingly to find the HOMO and LUMO for the system. When the excited state MO's are formed, the two-electron terms between the electron promoted to χ_r and the entire π -system, meaning the whole molecular orbital super-system are considered. This treatment allows the π -systems for all of the molecules in the simulation to be coupled together.

The excited-state transition-density matrix is formed by

$$\rho^{CI} = \sum_{nm}^{n_{ci}} C_{in}^* C_{jm} \phi_{in}^* \phi_{jm} \quad (2.23)$$

where the observables are the components of the CIS eigenvectors. The observables represent the configurations contribution to the wave function. The excited-state transition-density matrix can be decomposed into the the electron contribution to the virtual orbitals and the remaining hole contribution left in the occupied orbitals. The density matrix for the excited electron is found by

$$\rho_{rs}^{elec} = \sum_a C_{ra}^* C_{as} \phi_{ra}^* \phi_{as} \quad (2.24)$$

where the index r and s represents the virtual molecular orbitals and a and b represent occupied molecular orbitals. The density matrix for the hole is found by

$$\rho_{a,b}^{hole} = \sum_i C_{ai} C_{ib}^* \phi_{ai} \phi_{ib}^* \quad (2.25)$$

The ground-state Hartree Fock densities are found by

$$\rho_{a,b}^{HF} = \sum_k n_k \phi_{ak} \phi_{bk} \quad (2.26)$$

where n_k represents the electron occupation of orbital k . It is assumed that the electron density is excited from the Hartree-Fock ground state molecular orbitals and that the hole density resides in the valence band. With these assumptions,

we can add the excited-state electron density and simultaneously subtract the hole densities from the Hartree-Fock molecular orbitals. The electron density is modified in orbital basis and transformed into site basis, where the electron and hole densities are added and subtracted from specific $2p_z$ orbitals.

$$\rho^{EX} = \sum_{k=nl}^{occupied} n_k \phi_{ak} \phi_{bk} + \sum_a C_{ra}^* C_{as} \phi_{ra}^* \phi_{as} - \sum_i C_{ai} C_{ib}^* \phi_{ai} \phi_{ib}^* \quad (2.27)$$

Where k sums over the Hartree Fock orbitals of the system. The electron densities are removed from the Hartree Fock orbitals, starting from the lowest CI orbital to the HOMO. The excited electron densities are added to the virtual orbitals, starting from the LUMO to the highest CI orbital.

Chapter 3

Simulation

3.1 Introduction

In this chapter, we discuss how to use the π -MDX program. The π -MDX program was built on top of the TINKER MM/QM package. The basic procedure for creating a `.key` and `.xyz` file are described and many of the useful keywords used are introduced. The procedure for creating an `.xyz` file soaked in a solvent box is explained, along with some tips and common errors often encountered during the creation process. The modifications included in the π -MDX program are discussed and cataloged for future use. This chapter is intended to be a reference for future students interested in the π -MDX program.

3.2 TINKER XYZ and Key files

TINKER requires properly formatted `.xyz` and `.key` files. The `.xyz` file contains the coordinates and connectivities with the following format. The first line holds the total number of atoms in the system, the second line contains the starting of the information used by TINKER to describe the atoms in TINKER `.xyz` format, shown in Figure 3.1. The first column represents the atom number, which runs from 1 to the total number of atoms in the system. The second column is the atom symbol, taken from the MM3 parameter file `MM3.prm`. The third, fourth, and fifth columns are the x, y, and z components of the atoms positions. The sixth column is the MM3 atom type, these are found in the `MM3.prm` file. The last columns are the connectivities of the atoms, the connectivity of each atom must match what is expected for the MM3 atom type.

A sample `.key` file is shown in Figure 3.2. This contains all of the relevant information TINKER uses as input to run a simulation. The first row contains the keyword `parameters`, this keyword tells TINKER the path to the parameter file to be used in the simulation. The next lines contain the keyword `pisystem`, indicating the atoms in the `.xyz` file to include in the π -system. It must be noted that the length of each line in Fortran is finite, any text that exceeds the limit will be cut. The next three keywords, `A-AXIS`, `B-AXIS`, and `C-AXIS` give the initial values of the x, y, and z dimensions of the periodic simulation cell. Including this also tells TINKER

```

File Edit Options Buffers Tools Help
85 P3HT-PCBM
1 C -0.999000 0.968000 -5.863000 2 2 5 6
2 C -0.116000 0.296000 -6.716000 2 1 3 7
3 C 0.805000 1.193000 -7.274000 2 2 4 8
4 C 0.522000 2.421000 -6.672000 2 3 5 9
5 C -0.586000 2.290000 -5.836000 2 1 4 10
6 C -1.565000 0.380000 -4.761000 2 1 11 15
7 C 0.268000 -0.948000 -6.397000 2 2 12 13
8 C 2.084000 0.818000 -7.599000 2 3 14 20
9 C 1.511000 3.269000 -6.306000 2 4 18 19
10 C -0.655000 2.996000 -4.694000 2 5 16 17
11 C -1.081000 -0.901000 -4.446000 2 6 12 22
12 C -0.190000 -1.566000 -5.237000 2 7 11 23
13 C 1.584000 -1.337000 -6.570000 2 7 14 26
14 C 2.468000 -0.461000 -7.121000 2 8 13 35
15 C -1.699000 1.102000 -3.577000 2 6 16 21
16 C -1.165000 2.376000 -3.553000 2 10 15 29
17 C 0.364000 3.879000 -4.343000 2 10 18 36
18 C 1.435000 4.034000 -5.143000 2 9 17 40
19 C 2.821000 2.867000 -6.499000 2 9 20 41
20 C 3.094000 1.663000 -7.062000 2 8 19 37
21 C -1.207000 0.263000 -2.557000 2 15 22 27
22 C -0.877000 -0.976000 -3.093000 2 11 21 24
23 C 0.830000 -2.339000 -4.683000 2 12 25 26
24 C 0.160000 -1.710000 -2.605000 2 22 25 30
25 C 1.015000 -2.492000 -3.360000 2 23 24 59
26 C 1.942000 -2.164000 -5.509000 2 13 23 32
27 C -0.449000 0.722000 -1.520000 2 21 28 31
28 C -0.053000 2.040000 -1.482000 2 27 29 57
29 C -0.391000 2.865000 -2.496000 2 16 28 36
30 C 0.887000 -1.222000 -1.542000 2 24 31 33
31 C 0.592000 -0.026000 -0.958000 2 27 30 55
32 C 3.174000 -2.193000 -4.968000 2 26 34 60
33 C 2.163000 -1.710000 -1.701000 2 30 54 59
34 C 4.017000 -1.216000 -5.467000 2 32 35 45
UU:***-F1 pcbm.xyz Top Li (Fundamental)
Auto-saving...done

```

Figure 3.1: This is an example of the first page of a TINKER.xyz file. The first row shows the total number of atoms and the name of the molecules in file. The first column represents the atom number. The second column is the atom symbol. The third, fourth, and fifth column are the x, y, and z components of the atom. The sixth column is the MM3 atom type. The last columns are the connectivity of the atoms.

to apply periodic boundary conditions.

3.3 Creation of Simulation Cells and Solvent Boxes

The simulation cells were all carefully prepared with the minimization of kinetic energy in mind. The three simulation cells A, B, and C shown in Figure

```
Bitvise xterm - k2.chem.uh.edu:22
File Edit Options Buffers Tools Help
parameters ../../../../params/mm3 prm
pssystem 1225 1226 1227 1228 1229 1230 1231 1237 1238 1239 1240 1241 1242 1243
pssystem 1246 1247 1248 1249 1250 1251 1252 1253 1256 1257 1258 1259 1260 1261
pssystem 1262 1263 1266 1267 1268 1269 1270 1271 1272 1273 1293 1294 1295 1296
A-AXIS 2000
B-AXIS 28
C-AXIS 28
UU-:***-F1 3ppv2pcbm.key All L11 <Fundamental>
```

Figure 3.2: This is an example of a TINKER.key file. The first row contains the keyword `parameters`, this tells TINKER the path to the parameters file for the simulation. The keyword, `pssystem` tells TINKER which atom number in the `.xyz` file are going to be used for the π -system atoms. The next keywords, `*-AXIS` give the initial dimensions of the solvent box used for the `.xyz` file.

3.3, start as a cluster of PPV molecules that are stacked with a 10 Å gap in the X and Y direction between molecules. For simulation A and B, the PPV phase is ultimately intended to represent the interface between two large bulk phases forming an interface, similar to a by-layer heterojunction. In simulation C the PPV molecules are set into a 5×5 evenly spaced square grid. All of the PPV cells are initially run through a NPT ensemble at 100 K and 10,000 ATM using only MM. This step reduces

the cells sizes, compressing the cells until the density of the PPV molecules are close to that of solid PPV 1.63 g/cm^3 . The cells are then placed into a 10,000 fs, 1 fs time step MM simulation using the NVT ensemble, allowing the PPV molecules to relax and find the equilibrium distance between one another inside the new solvent box size. For simulation, A and B the PCBM cells are created and compressed such that the solvent box boundary conditions match thoughts of the PPV systems solvent box. These simulation cells are adjoined such that the broad side of the PPV molecules are facing the PCBM, making a by-layer simulation cell with a definite PPV/PCBM interface. For simulation C, the PPV cell is soaked into the larger PCBM solvent box. The PCBM molecules overlapping the PPV system are moved to the edge of the box, this create a definite phase separation that looks like a blended heterojunction. The three merged cells are next run through a MM NPT simulation, using the same parameters as the previous NPT simulation, compressing the cell until the density is again close to that of solid PPV. Next, the three simulation cells are allowed to equilibrate during a 10,000 fs, 1 fs time step MM simulation using a NVT ensemble allowing the molecules at the interface to interact and find new equilibrium positions. The three blended cells are next run through an energy minimization subroutine to find the local minima in the potential energy surface. Next the π -active system is activated and a 1,000 fs, 1 fs time step ground-state NVT-simulation is run allowing the π -active molecules to adjust to the π -system. The simulation cell is next run through an 1,000 fs, 1 fs time step excited-state calculation, using the NVT ensemble. This allows the system to relax the electron and hole within the donor/acceptor system. At this point, the local bond orders are modified by the bond-charge matrix

and the molecules need some time to relax and find new equilibrium bond orders between the effected C-C bonds. This step is taken because the molecule that is excited initially goes through a rapid change in electronic configuration. This can cause the total energy of the cell to increase rapidly if the molecules are packed too tightly. Should the simulation crash, the solvent box needs to be increased by a small amount and the preparation steps repeated. The PPV bulk and π -active region of simulation C can be seen in Figure 3.4. Adhering to this procedure, greatly reduces the relaxation time and simulation time needed for a long simulation. Simulations A and C contain over 5000 atoms, with a π -system containing over 300 π -active electrons and a simulation time of 50,000 fs.

3.4 Generating the Fock Matrix

Inside of the π -MDX source directory, the `piscf.f` file holds the heart of our calculations. The first step is to compute the Fock matrix and find the ground-state molecular orbitals. The H^{core} integrals must be calculated first, so that they can be used as the initial guess at the Fock matrix for the SCF procedure. The PPP Hamiltonian is introduced, reducing the H^{core} integrals into two parts. The first is the one-electron Hamiltonian, `hc(i,i)`, containing the kinetic energy and the interaction with it's own nuclei. This term is uniform and can be taken as the same for all identical C=C hydrocarbons in the system. These interactions representing the kinetic energy and the one-center Coulomb integral are calculated by a semi-empirical method

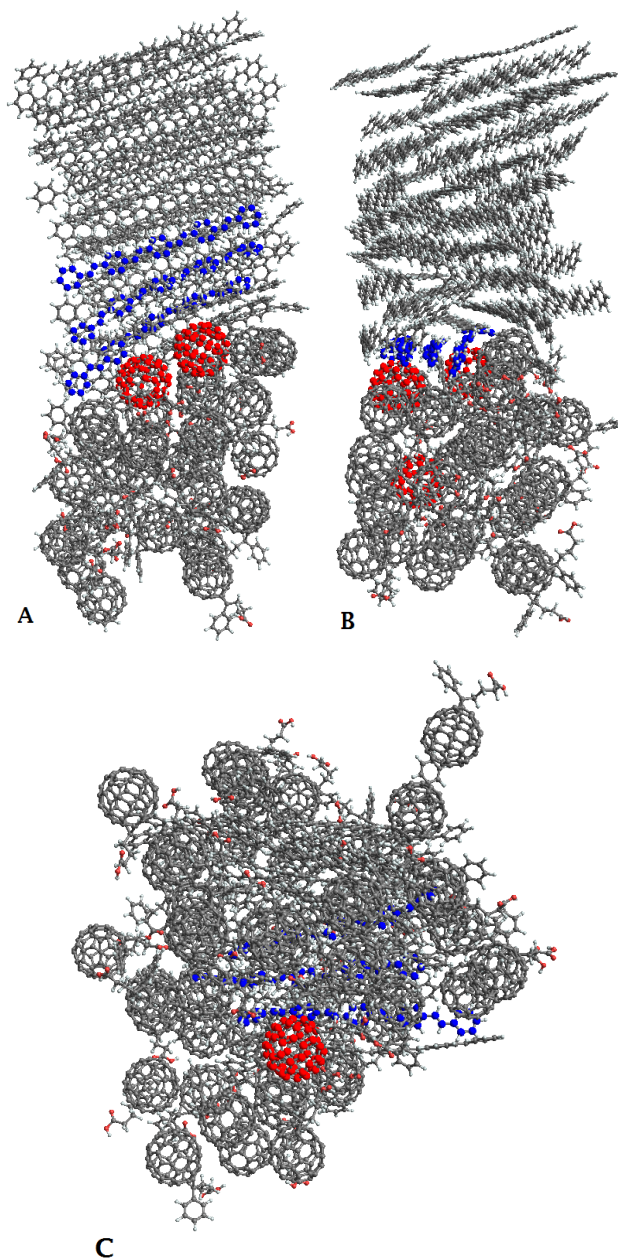


Figure 3.3: Snapshot of the three MD simulation cells: A, B, and C. A and B contain 30 PCBM molecules and 50 PPV oligomers following equilibration at 100 k and 1 ATM of pressure. C contains 50 PCBM molecules and 25 PPV oligomers following equilibration at 100 K and 1 ATM of pressure. The red and blue highlighted molecules denote the π -active units in our system.

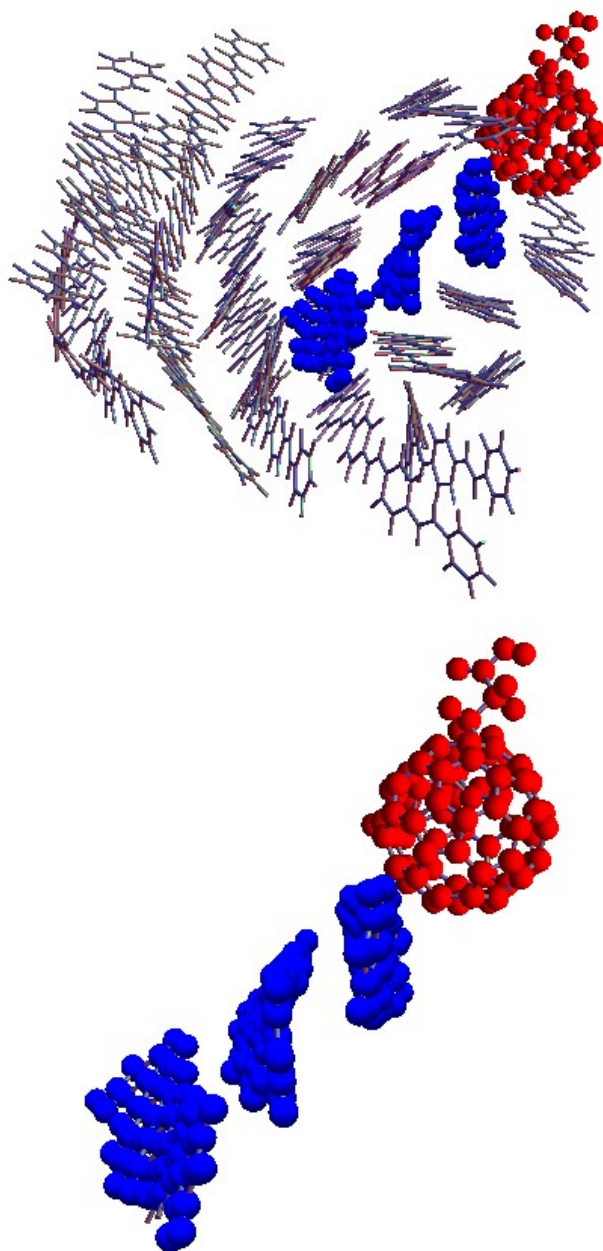


Figure 3.4: The π -active region is shown in the 5×5 bulk PPV portion. The non- π -active PCBM solvent molecules have been removed, showing how the bulk PPV region reacted to the procedure for creation of a simulation cell. The picture is centered on the central blue PPV molecule, looking directly down its axis. The molecules with blue spheres (PPV) represent donor molecules while the molecule with red spheres (PCBM) represent acceptor molecule.

$$\text{IP}(i) = W(i) + (1 - q(i) * \text{em}(i)) \quad (3.1)$$

Where $W(i)$ is the ionization potential of atom i , $q(i)$, is the π -contribution of atom i , and $\text{em}(i)$ is the inter-nuclear Coulomb repulsion for atom i and are stored in $\text{ip}(i)$. The full H_{uv}^{core} diagonal terms are given by

$$\text{hc}(i, i) = \sum_{i,j}^{\text{norbit}} \text{IP}(i) - q(j) * \gamma(i, j) \quad (3.2)$$

Where $\gamma(i, j)$ are the two-center repulsion integral between neighboring atoms i and j . The two-center repulsion integrals $\gamma(i, j)$ are calculated by

$$1/\sqrt{\text{rijsq}^2 + \text{g11sq}^2}. \quad (3.3)$$

Where rijsq are the squares of the x, y, and z components of the vector between i and j . The off-diagonal elements of the H_{uv}^{core} are calculated separately using Ohno's two-center repulsion integrals. The one-center repulsions integral, where the potential due to the electron interacting with it's own core are stored in g11 . These two-center values are stored in g12 . The C-C resonance integrals are calculated using the Whitehead and Lo formula, the bond energies are computed using a semi-empirical method based on the Morse potential.

$$\text{ebond} = (2e^{\text{abnz}(\text{blb}-r_{ij})} - e^{2(\text{abnz}(\text{blb}-r_{ij}))})\text{ebb} \quad (3.4)$$

$$\text{eebond} = (2e^{\text{aeth}(\text{ble}-r_{ij})} - e^{2(\text{aeth}(\text{ble}-r_{ij}))})\text{ebe} \quad (3.5)$$

Where `abnz` and `aeth` represent PPP constants in benzene and ethylene, `blb` and `ble` represent the equilibrium-bond lengths for benzene and ethylene, `ebb` and `ebe` are the equilibrium-bond energies for benzene and ethylene. These values are specified at the beginning of the `piscf.f` file and are constants shown in Table 2.1. The individual matrix elements of the $H_{i,j}^{core}$ matrix between bonded atom i and j are

$$hc(i, j) = 1.5(\text{bebond} - \text{eebond}) - \frac{3}{8}g11 + \frac{5}{12}g12 - \frac{1}{24}g14 \quad (3.6)$$

The total H^{core} matrix is used as the initial guess for the Fock matrix in the SCF procedure. The `pitilt` subroutine, calculates the overlap integral between bonded sites. This reduces the two electron integrals between non bonded sites to zero except for the one-center exchange repulsion. Upon convergence the Fock matrix is diagonalized by calling the subroutine `jacobi`. The Fock molecular orbitals are then generated and stored in `v(i, j)`. The Hartree-Fock ground-state energy (`hfen`) is calculated by summing the molecular-core integrals (`xi`), molecular Coulomb repulsion integrals (`xj`), molecular-exchange repulsion integrals (`xk`), and the nuclear repulsion (`xg`).

3.5 Generating the CIS Matrix

The CIS matrix is scaled by two terms, “nl” and “nu”. These values are hard-coded into the CI portion of the `piscf.f` file and control the size of the CIS space. The variables “nl” and “nu” stand for “number of molecular orbitals lower” and

“number of molecular orbitals higher” than the band gap. The size of the CIS space “nci” is given by “nl” \times “nu”. The functions `iconfig(m,1)=i` and `iconfig(m,2)=j` generate the singly excited CIS configurations, where `iconfig(m,1)=i` forms the rows and `iconfig(m,2)=j` forms the columns for the CIS matrix.

$$\begin{pmatrix} \langle \Psi_1^1 | H | \Psi_1^1 \rangle & \langle \Psi_1^1 | H | \Psi_1^2 \rangle \\ \langle \Psi_1^2 | H | \Psi_1^1 \rangle & \langle \Psi_1^2 | H | \Psi_1^2 \rangle \end{pmatrix}$$

The Hamiltonian can be found by evaluating the matrix elements of the system between determinants. For determinants of one-electron operators in terms of spin orbitals, there are three distinct cases. Case 1 is where the matrix element does not differ in spin orbitals at all, this yields the matrix elements $-h_{11} + h_{22} - J + K$. For case 2, where the matrix elements differ in one spin orbital, the matrix elements are $-h_{12} + J - K$ for $r = s$ and $h_{12} - J + K$ for $a = b$. For case 3, where the matrix elements differ in two spin orbitals, the matrix elements are $-J + K$. Where h is the single electron term, J is the Coulomb repulsion, and K is the exchange energy. Evaluating the matrix elements of the CIS matrix yields

$$\begin{pmatrix} -h_{11} + h_{22} - J + K & -J + K \\ -J + K & -h_{11} + h_{22} - J + K \end{pmatrix}$$

Inside the π -MDX code, we couple the various CIS configurations together by calculating all of the Coulomb and exchange integrals between molecular orbitals inside of each configuration. This allows for electron density to be moved between sites in the excited state of the entire π system. This is prohibited in the ground state because the PPP Hamiltonian enforces neglect of differential overlap and coupling terms between nonbonded sites are neglected. The configurations are cumulated into

the matrix `sing(i,i)` as shown in Equation 2.1. The diagonal elements of this matrix have the band-gap energy added to the singlet energy. The matrix `sing(i,j)` is diagonalized using the subroutine `jacobi`. This yields the excited state molecular orbitals `vs(i,j)` and the orbital energies `ens`. The excited-state transition-density matrix `dens(i,j)` are constructed from the CI coefficients. The matrix `dens(i,j)` is set up such that the rows i corresponds to the probability for an electron to occupy a specific orbital on i , while j gives the probability that the hole will occupy a specific orbital on j with the electron located on any other orbital. The excited state electron density matrix `e(i)` is calculated by

$$\mathbf{e}(i) = \sum_j^{\text{norbit}} \text{dens}(i,j)^2 \quad (3.7)$$

The hole density matrix `h(i)` is found by summing over i . The Hartree Fock orbitals are found by

$$\text{hfoc}(i) = 2 \sum_j^{\text{nfill}} \sum_k^{\text{norbit}} v(i,k)v(j,k) \quad (3.8)$$

These equations are in orbital basis and can be combined and converted into a modified bond charge matrix in site representation by

$$\text{tranvect}(i,j) = \sum_i^{\text{norbit}} \sum_j^{\text{norbit}} \sum_k^{\text{norbit}} (\text{hfoc}(k) - \mathbf{h}(k) + \mathbf{e}(k))v(i,k)v(j,k) \quad (3.9)$$

Where `tranvect(i,j)` is the new bond charge-density matrix for the excited state

system. For more information on CIS and the formation of the electron and hole-density matrix, the book Modern Quantum Chemistry [53] contains a comprehensive review.

3.6 Then Bond Charge Matrix and MM

The trace of the bond charge-density matrix gives the total charge in the system while, the off-diagonal elements represent the change in bond order due to the transfer of electron density between sites. The electron occupancy `elec(i,j)` and hole occupancy `hole(i,j)` are determined using Equation 2.24 and 2.25. The total bond charge-density matrix `tranvect(i,j)` is given by Equation 3.9. The new modified bond charge-density matrix takes into account electron density that has been promoted into the conduction band and the corresponding hole density that is left in the valence band. It is important to note that `hfoc(i,j)` is block diagonal between π -active molecules, due to the neglect of differential overlap. The migration of electron density occurs due to the Coulomb potential included in the formation of the excited-state wave function.

Accounting for the addition and subtraction of electron densities, the bond-charge matrix gives us the ability to modify the local equilibrium bond orders inside the MM portion of the code. The equilibrium bond orders between atoms, “i” are modified by

$$\text{BO}_i = \sum_i^{\text{nbpi}} [\text{I}_{\text{BO}}(i) + \text{T}_{\text{BO}}(1 - \text{P}(i))] \quad (3.10)$$

where the sum over `nbpi` represents a change in all of the listed π bonds. $\text{I}_{\text{BO}}(i)$ is the initial bond length for a π bond order of one between the two specified atom types in the parameter file. $\text{T}_{\text{BO}}(i)$ is the rate of bond length increase with bond order decrease and $\text{P}(i)$ is the bond length between the specified sites in the bond-charge matrix. A plot of the change in bond length as the bond order decreases is shown in Figure 3.5. BO_i is used for the new bond order in the MM portion of the code. In a very similar fashion, the bond stretch force constants between π -active C - C bonds are also allowed to vary with bond order from there initial MM value.

$$\text{BK}_i = \sum_i^{\text{nbpi}} [\text{K}_{\text{BK}}(i) + \text{O}_{\text{BK}}(1 - \text{P}(i))] \quad (3.11)$$

In this equation as in the previous, $\text{K}_{\text{BK}}(i)$ represents the bond stretch force constant between the specified atoms. O_{BK} is the rate of force constant decrease with bond order decrease and P_i are the bond orders between the specified sites in the bond-charge matrix. A plot of the change in force constant as the bond order decreases is also shown in Figure 3.5. In essence we are using the QM electron density calculated to modify the values of the bond order and force constants produced from the classical MM calculation.

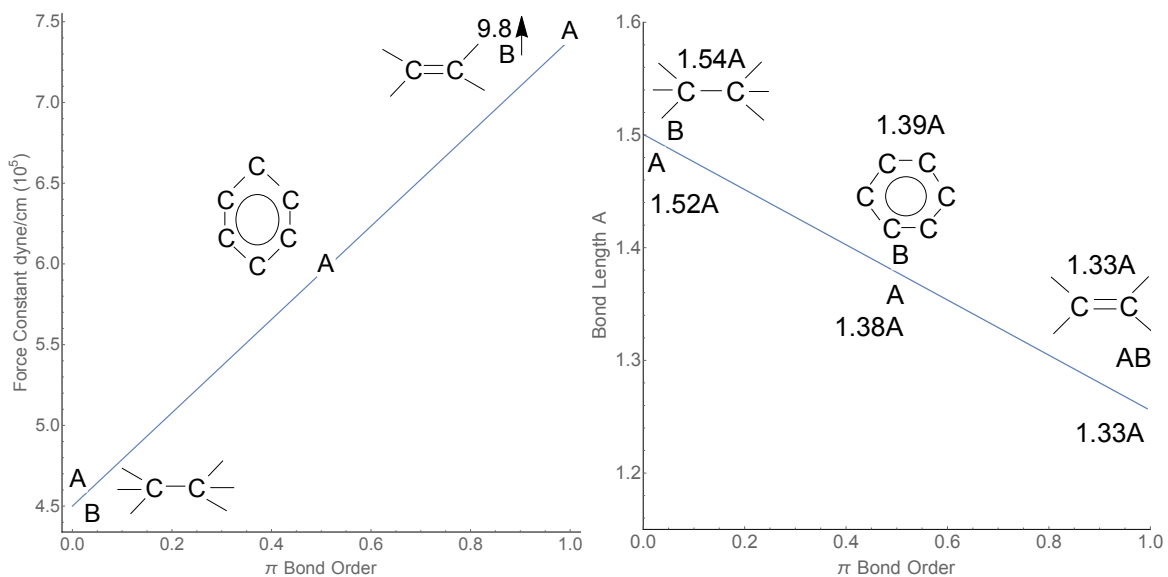


Figure 3.5: These graphs show a plot of how the local π -bond order affects the bond stretch force constant and the equilibrium bond lengths of the system. They are generated by manually changing the value of $P(i)$ in Equations 3.10 and 3.11 for ethylene. The values shown are the actual values for the new bond order and force constant that are feed into the MM portion of π -MDX. The equilibrium bond lengths and force constants found in the MM3 parameter set are shown by the large A's. Experimental values for the bond lengths and force constants [54] are shown as large B near the structure of the molecule they were taken from.

Chapter 4

Structural Fluctuations and Environmental Noise in the Electron/Hole Separation Kinetics at Organic Polymer Bulk-Heterojunction Interfaces

1

¹This chapter is taken from the following publication
[66] E. R. Bittner and A. C. Kelley. The role of structural fluctuations and environmental noise in the electron/hole separation kinetics at organic polymer bulk-Heterojunction interfaces. *PCCP*, pages 28853-28859, 2015.

4.1 Introduction

Organic semi-conducting polymers are currently of broad interest as potential low-cost materials for photovoltaics. Studies into the fabrication, chemistry, and fundamental physics of these materials continue to advance, hence organic photovoltaics have begun to appear in the modern market place. Composite materials fabricated by mixing semi-conducting polymers with different electron and hole accepting properties have been used to produce efficient photovoltaic cells under standard solar illumination. [55, 56, 57] The power conversion efficiencies of highly optimized organic polymer-based photovoltaic cells routinely exceed 10 % with reports of efficiencies as high as 12 % in multi-junction organic photovoltaics. The primary charge carrier in organic photovoltaic materials are excitons, electron/hole pairs bound by Coulombic attraction, rather than acting as free charges. This causes the efficiency of organic photovoltaics to be considerably lower than other forms of solar cells, however, the boost in efficiency indicates that mobile charge carriers can be generated efficiently in well-optimized organic heterostructures. In spite of vigorous, multidisciplinary research activity the underlying photo-physical mechanism for converting highly-bound molecular (Frenkel) excitons into mobile and asymptotically free photocarriers remains elusive. [28, 58, 59, 60, 39]

The generic photophysical pathways that underlie the generation of mobile charge

carriers in organic photovoltaic solar cells are sketched in Figure 1.4. The absorption of a photon by the material produces a π to π^* excitation (exciton) within the bulk (a) that can migrate and diffuse via Forster energy-transfer processes. Once in close proximity to a bulk-heterojunction interface, energetic off-sets between the respective HOMO and LUMO levels of adjacent donor and acceptor molecules provide the necessary driving force to separate an exciton into a localized charge transfer (CT) state (b) which typically lies in the range of 0.25 to 0.4 eV lower in energy. Alternatively, an exciton may dissociate directly via tunneling into charge-separated (CS) or polaron states (d) which may subsequently evolve to contribute to the photocurrent or undergo geminate or non-geminate recombination to form CT states (d). We distinguish CT states from CS states by whether or not the donor and acceptor species are in direct contact (CT) or separated by one or more intermediate molecules (CS).

Ultrafast spectroscopic measurements on organic photovoltaic systems have reported that charge photoexcitations are generated on ≤ 100 -fs [11, 16, 24, 25, 26, 27, 28] timescales; however, full charge separation to produce free photocarriers is expected to be energetically expensive given the strong coulombic attraction between electrons and holes due to the low dielectric constant in molecular semiconductors. Nonetheless, experiments by Gelinis *et al.*, in which Stark-effect signatures in transient absorption spectra were analysed to probe the local electric field as charge separation proceeds, indicate that electrons and holes separate by as much as 40 Å over the first 100 fs and evolve further on pico-second time scales to produce unbound and hence freely mobile charge pairs. [10] Concurrently, transient

resonance-Raman measurements by Provencher *et al.* [15] demonstrated clear polaronic vibrational signatures on sub-100 fs on the polymer backbone, with very limited molecular reorganization or vibrational relaxation following the ultrafast step. Such rapid through-space charge transfer between excitons on the polymer backbone and acceptors across the heterojunction would be difficult to rationalize within Marcus theory using a localized basis without invoking the unphysical distance dependence of tunneling-rate constants [29] and appear to be a common feature of organic-polymer bulk-heterojunction systems.

Polymer micro-structural probes have revealed general relationships between disorder, aggregation and electronic properties of polymeric semiconductors. [21] Moreover, aggregation (ordering) can be perturbed by varying the blend-ratio and composition of donor and acceptor polymers. [9] On one hand, energetic disorder at the interface would provide a free-energy gradient for localized charge-transfer states to escape to the asymptotic regions. In essence, the localized polarons in the interfacial region could escape into bands of highly mobile polarons away from the heterojunction region. [61, 62, 63] On the other hand, energetic disorder in the regions away from the interface would provide an entropic driving force by increasing the density of localized polaron states away from the interfacial region, allowing the polarons to hop or diffuse away from the interface before recombination could take place. [23] It has also been suggested that in polymer/fullerene blends, interfacial exciton fission is facilitated by charge-delocalisation along the interface which provides a lower barrier for fission with the excess energy provided by thermally-hot vibrionic dynamics. [18]

Finally, a report by Bakulin *et al.* indicates that when relaxed charge-transfer excitons are pushed with an infrared pulse, they increase photocurrent via delocalised states rather than by energy gradient-driven hopping. [64]

Recent MD Simulations by Fu *et al.* of a model Squaraine/Fullerene OPV cell indicate that the degree of disorder at the interface directly affects couplings and hence golden-rule transition rates between the ground and excited states. The disorder in the system is at least partly introduced by thermal annealing and the interactions between the Squaraine and Fullerene layers. Their simulations indicate that even at 300 K, the thermal motions of the molecules at the interface can be quite profound and the degree of disorder inherent around the interface can greatly affect the formation of electron/hole pairs. [65]

Bittner *et al.* [40] recently presented a fully quantum dynamical model of photo-induced charge-fission at a polymeric type-II heterojunction interface. The model supposes that the energy level fluctuations due to bulk atomic motions create resonant conditions for coherent separation of electrons and holes via long-range tunneling. Simulations based upon lattice models reveal that such fluctuations lead to strong quantum mechanical coupling between excitonic states produced near the interface and unbound electron/hole scattering states resulting in a strong enhancement of the decay rate of photoexcitations into unbound polaronic states.

In the succeeding sections, we employ an atomistic quantum/molecular dynamics study of a model donor-acceptor blend to provide an estimate of the interstate transition rates with the excited-state manifold. Our simulations combine a molecular dynamics description of the atomic motions coupled to a description of the excited

state π -electronic structure. By analyzing the energy gap fluctuations between excited states, we provide a robust estimate of both the interstate electronic couplings, decoherence times, and transition rates. We begin with a brief overview of our model and then describe our results.

4.2 A Model Two Level System

A simple model for considering the role of the interaction between the environment and the π to π^* transition can be developed as follows. [66, 67, 68] Consider a two-state quantum system with coupling λ in which the energy gap $\Delta(t)$ fluctuates in time about its average Δ_0 and $\langle \Delta(t)\Delta(0) \rangle = \sigma_\Delta^2$, shown in Figure 4.1. In a two-state basis of $|0\rangle, |1\rangle$ the Hamiltonian for this can be written as

$$H = \frac{\Delta(t)}{2}\hat{\sigma}_z + \lambda\hat{\sigma}_x \quad (4.1)$$

where $\hat{\sigma}_z$ and $\hat{\sigma}_x$ are Pauli matrices. Note that Equation 4.1 can be transformed such that fluctuations are in the off-diagonal coupling

$$H = \frac{\Delta_0}{2}\hat{\sigma}_z + \delta V(t)\hat{\sigma}_x \quad (4.2)$$

where $\Delta_0 = \bar{\Delta} + \lambda$ and $\delta\bar{V}(t) = 0$. The fluctuations in the electronic energy levels are attributed to thermal and bond-vibrational motions of polymer chains and can be related to the spectral density, $S(\omega)$ via

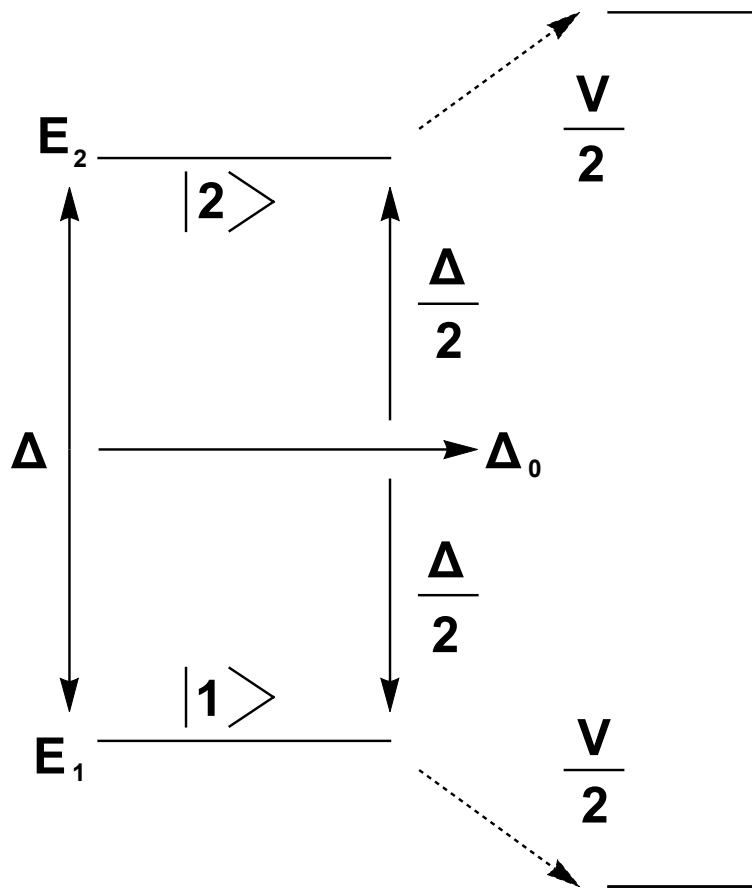


Figure 4.1: A two level system between states $|1\rangle$ and $|2\rangle$ with an average energy gap Δ_0 . The energy gap is given by Δ where λ is the coupling between $|1\rangle$ and $|2\rangle$.

$$\bar{V}^2 = \delta\bar{V}^2(t) = \int_{-\infty}^{+\infty} \frac{d\omega}{2\pi} S(\omega). \quad (4.3)$$

Taking the determinate of Equation 4.2 and averaging over the environmental noise, we can write the average energy gap from Δ_0 as $\hbar\bar{\Omega} = \pm\sqrt{\Delta_0^2 + \bar{V}^2}$ with eigenstates

$$|\Psi+\rangle = \cos\theta|0\rangle + \sin\theta|1\rangle \quad (4.4)$$

$$|\Psi-\rangle = -\sin\theta|0\rangle + \cos\theta|1\rangle$$

where $\tan 2\theta = |\bar{V}|/\Delta_0$ defines the mixing angle between original kets. The new states $|\Psi+\rangle$ and $|\Psi-\rangle$ are linear combinations of the original states $|1\rangle$ and $|2\rangle$ as shown Figure 4.1. When the energy gaps $V \ll (\Delta)/2$, $\tan 2\theta = V/((\Delta)/2)$ becomes small and $\theta \rightarrow 0$. In this limit, the eigenstates become more and more like the initial states $|1\rangle$ and $|2\rangle$. In the other limit, as $(\Delta)/2 \rightarrow 0$ and the initial states become degenerate, $\tan 2\theta$ diverges and $\theta = \pi/4$. In this case, the system is brought into a strong coupling regime and the true eigenstates of the system are the totally mixed states. Consequently, by analyzing energy-gap fluctuations, we can obtain an estimate of both the coupling between states as well as transition rates.

4.3 Noise Averaged Kinetics

To estimate the average transition rate between states, we first consider the Hamiltonian for a two level system.

$$H = \frac{\Delta}{2} \begin{pmatrix} 1 & 0 \\ 0 & -1 \end{pmatrix} + \frac{\hbar\lambda}{2} \begin{pmatrix} 0 & 1 \\ 1 & 0 \end{pmatrix}$$

The time derivative of the density operator must be found such that the equations of motion for the density-matrix elements can be determined. The density operator

$$\hat{\rho}(t) = |\Psi(t)\rangle\langle\Psi(t)| \quad (4.5)$$

where the time derivative is

$$i\hbar \frac{\partial}{\partial t} \rho = i\hbar \frac{\partial}{\partial t} |\Psi(t)\rangle\langle\Psi(t)| + |\Psi(t)\rangle\langle\Psi(t)| i\hbar \frac{\partial \langle\Psi(t)|}{\partial t} \quad (4.6)$$

where $i\hbar \frac{\partial |\Psi(t)\rangle}{\partial t} = H |\Psi(t)\rangle$ and $i\hbar \frac{\partial \langle\Psi(t)|}{\partial t} = -\langle\Psi(t)| H$. So taking the time derivative of the density matrix $i\hbar \frac{\partial}{\partial t} \rho$ is equivalent to taking the commutator $[H, \rho]$. Working through the time derivative gives the equations of motion for the density-matrix elements

$$\dot{\rho}_{11} = -\frac{i}{\hbar} \lambda (\rho_{21} - \rho_{12}) \quad (4.7)$$

$$\dot{\rho}_{22} = \frac{i}{\hbar} \lambda (\rho_{21} - \rho_{12})$$

$$\dot{\rho}_{12} = -\frac{i}{\hbar} \lambda (\rho_{22} - \rho_{11})$$

$$\dot{\rho}_{21} = \frac{i}{\hbar} \lambda (\rho_{22} - \rho_{11})$$

These equations can to be solved by taking time derivative of $\dot{\rho}_{11}$

$$\ddot{\rho}_{11} = i\lambda(\dot{\rho}_{12} - \dot{\rho}_{21}) = -2\lambda^2(\rho_{11} - \rho_{22}) \quad (4.8)$$

Since $\rho_{11} + \rho_{22} = 1$ Equation 4.8 becomes the differential equation

$$\ddot{\rho}_{11} = -2\lambda^2 - 4\lambda^2\rho_{11} \quad (4.9)$$

Solving the differential equation produces

$$\rho_{11}(t) = \frac{1}{2} + C_1\cos(2\lambda t) + C_2\sin(2\lambda t) \quad (4.10)$$

Setting the density in the ground state initially to one, $\rho_{11}(0) = 1$ yields

$$\rho_{11}(t) = \cos^2(\lambda t) \quad (4.11)$$

$$\rho_{22}(t) = \sin^2(\lambda t) \quad (4.12)$$

for the populations of the ground and excited state. The couplings between states can now be solved using to find ρ_{12}

$$\begin{aligned} \int_0^t \dot{\rho}_{12}(t)dt &= i\lambda \int_0^t \cos^2(\lambda t) - \sin^2(\lambda t)dt \\ &= \frac{i}{2} \sin(2\lambda t) \end{aligned} \quad (4.13)$$

The time evolution of the populations show that at $t\lambda = 0$ the population is all located in state one and is transferred to state two at $t\lambda = \pi/2$. This type of periodic system oscillates between state one and state two at a Rabi frequency $\Omega = \lambda/\hbar$. It must be noted that in order to transfer population from state one to state two, you must first establish the coherence ρ_{12} and ρ_{21} between the two states. This system is completely reversible until you allow the coherence to be destroyed by coupling the system to the environment.

In a thermal system, energy transfer can be irreversible due to the contact and mixing between donor and acceptor species with solvent media. For a system soaked in an environment, we need to consider the relaxation populations and coherences in their equilibrium values. The new time derivative of the density operator taking into account the relaxation and coherences are given by

$$\frac{\partial \rho_{ii}}{\partial t} = \frac{1}{i\hbar} [H, \rho]_{ii} + \frac{1}{T_1} (\rho_{ii}^{(eq)} - \rho_{ii}) \quad (4.14)$$

$$\frac{\partial \rho_{ij}}{\partial t} = \frac{1}{i\hbar} [H, \rho]_{ij} - \frac{1}{T_d} (\rho_{ij}) \quad (4.15)$$

for the diagonal and off-diagonal terms. The relaxation time T_1 represents the time scale for the populations of each state to relax to its equilibrium value. The decoherence time, T_d , represents the the decoherence time for the quantum superposition, which in turn, can be related to the spectral density via $T_d^{-1} = \lambda/\hbar$. The equations of motion for the two level system coupled to the environment are given by

$$\begin{aligned}
\dot{\rho}_{11} &= -\frac{i}{\hbar}\lambda(\rho_{21} - \rho_{12}) - \frac{1}{\tau_1}\rho_{11} \\
\dot{\rho}_{22} &= \frac{i}{\hbar}\lambda(\rho_{21} - \rho_{12}) - \frac{1}{\tau_2}\rho_{22} \\
\dot{\rho}_{12} &= -\frac{i}{\hbar}\lambda(\rho_{22} - \rho_{11}) - \frac{1}{T_d}\rho_{12} - \frac{\Delta}{i\hbar}\rho_{12} \\
\dot{\rho}_{21} &= \frac{i}{\hbar}\lambda(\rho_{22} - \rho_{11}) - \frac{1}{T_d}\rho_{21} + \frac{\Delta}{i\hbar}\rho_{21}
\end{aligned} \tag{4.16}$$

where τ_1 and τ_2 represent the radiative lifetimes of exciton's located in state one and two. Taking T_d to be short compared to the lifetimes of the exciton's, we can write the population of the initial state as

$$\rho_{11}(t) = \exp\left[-\left(\frac{1}{\tau_1} - k\right)t\right] \tag{4.17}$$

where k is the average state-to-state transition rate. Integrating this over time, we obtain an equation of the form

$$\int_0^\infty \rho_{11}(t)dt = \left(\frac{1}{\tau_1} + k\right)^{-1} \tag{4.18}$$

suggesting a form for the exact solution of Equation 4.16. Taking the Laplace transform of Equations 4.16 and assuming that our initial population in state one ($\rho_{11}(0) = 1$), Equations 4.16 become a series of algebraic equations

$$-1 = -\frac{i}{\hbar}\lambda(\tilde{\rho}_{21} - \tilde{\rho}_{12}) - \frac{1}{\tau_1}\tilde{\rho}_{11} \tag{4.19}$$

$$\begin{aligned}
0 &= \frac{i}{\hbar} \lambda (\tilde{\rho}_{21} - \tilde{\rho}_{12}) - \frac{1}{\tau_2} \tilde{\rho}_{22} \\
0 &= -\frac{i}{\hbar} \lambda (\tilde{\rho}_{22} - \tilde{\rho}_{11}) - \frac{1}{T_d} \tilde{\rho}_{12} - \frac{\Delta}{i\hbar} \tilde{\rho}_{12} \\
0 &= \frac{i}{\hbar} \lambda (\tilde{\rho}_{22} - \tilde{\rho}_{11}) - \frac{1}{T_d} \tilde{\rho}_{21} + \frac{\Delta}{i\hbar} \tilde{\rho}_{21}
\end{aligned}$$

which after a bit of algebra gives a rate constant of the form

$$k = 2 \frac{\lambda^2}{\hbar^2} \frac{T_d}{(T_d \Delta_0 / \hbar)^2 + 1} \quad (4.20)$$

The average rate vanishes in the limit of rapid decoherence ($T_d \rightarrow 0$). This is the quantum Zeno effect whereby rapid quantum measurements on the system by the environment at a rate given by T_d^{-1} collapses the quantum superposition formed due to the interactions and thereby suppresses transitions between states. On the other hand, transient coherences can facilitate quantum transitions between otherwise weakly coupled states.

For the sake of connecting this to the photophysical dynamics of an organic photovoltaic heterojunction, let us assume that one state corresponds to a charge-transfer state and the other corresponds to a charge-separated state. When the fluctuations are weak, $\lambda \ll \Delta_0$, the original kets $|CT\rangle$ and $|CS\rangle$ provide a good zeroth description of actual eigenstates of the system and the coupling can be treated as a weak perturbation. However, when the off-diagonal couplings are comparable to the average gap, even low-lying charge-transfer states may be brought into strong coupling with the charge-separated states.

The implication of this heuristic model is that one can obtain the input to the rate

equation given by Equation 4.20 from mixed quantum classical simulations that take into account the excited state populations. Here we report on such simulations of a model organic photovoltaic system consisting of a blend of fullerene and polyphenylene vinylene oligomers. Our simulation method employs an atomistic description of the nuclear dynamics described by a force-field that responds to changes in the local π electronic structure of a sub-set of molecules within the simulation cell. We restrict the excited-state population to the lowest π to π^* excitation as to simulate the long-time fate of a singlet charge-transfer state prepared via either photoexcitation or charge recombination. By analyzing the energy gaps between electronic adjacent states and the character of the excited states in terms of electron/hole configurations, we can deduce how small vibrionic motions of the polymer chains modulate the electronic coupling and induce charge-separation.

4.4 Methods

Our simulations employ a modified version of the TINKER (MD) package [50, 69] in which the MM3 [70] intramolecular bonding parameters were allowed to vary with the local π -electronic density as described by a (PPP) semi-empirical Hamiltonian. [71, 72] Specifically, we assume that the internal bond force constants, bond-lengths, bond angle, bending potentials, and bond torsion parameters are linear functions of the local bond-order. We specifically chose one PCBM and three nearby PPV oligomers to represent a model bulk-heterojunction in order to study the penetration of extended intramolecular electronic states into the bulk region.

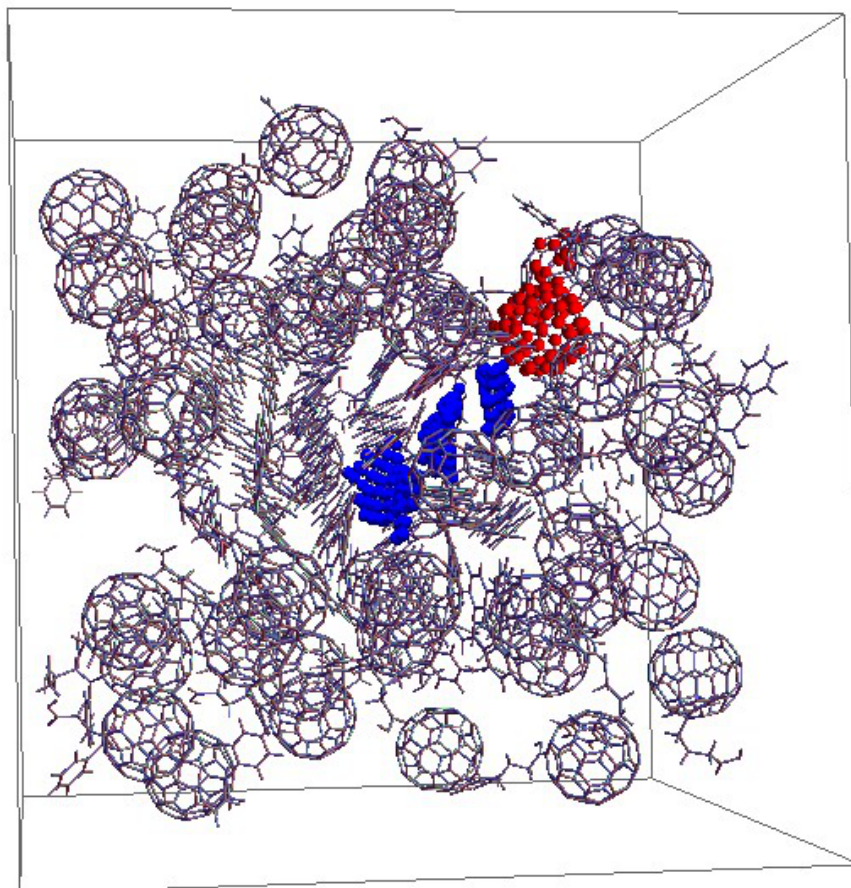


Figure 4.2: Snapshot of the MD simulation cell containing 50 PCBM molecules and 25 PPV oligomers following equilibration at 100 K and 1 ATM of pressure. The blue and red highlighted molecules denote the π -active donor/acceptor units in our system.

The remaining molecules in the simulation were treated using purely classical force-field. At each step of the simulation, we compute the Hartree-Fock ground-state for the π system and use (CIS) to describe the lowest few $\pi \rightarrow \pi^*$ excitations. Intermolecular interactions within the active space were introduced via non-bonding Coulombic coupling terms and static dispersion interactions contained within the MM3 forcefield.

Figure 4.2 shows a snapshot of the periodic simulation cell containing fifty PCMB molecules and twenty five PPV oligomers following equilibration at 100 K and 1 ATM of pressure using classical molecular dynamics (MD) within the NPT ensemble. The molecules surrounding the four π -active molecules serve as a thermal bath and electronic excitations are confined to the π -active orbitals. In total, our π -active space included a total of 172 carbon $2p_z$ orbitals and we used a total of ten occupied and ten unoccupied orbitals to construct electron/hole configurations for the CI calculations. During the equilibration steps, we assume the system to be in its electronic ground state, after which we excite the system to the first CIS excited state and allow the system to respond to the change in the electronic density within the adiabatic/Born-Oppenheimer approximation. It is important to note that the excited state we prepare is not the state which carries the most oscillator strength to the ground nor do we account for non-adiabatic surface hopping-type transitions in our approach. [73, 74, 75] Our dynamics and simulations reflect the longer-time fate of the lowest-lying excited state populations as depicted in step (d) in Figure 1.4. The combination of a classical MD forcefield with a semi-empirical description of a select few molecules within the system seems to be a suitable compromise between a fully *ab*

initio approach which would be limited to only a few molecules and short simulation times and a fully classical MD description which would neglect any transient changes in the local electronic density [26]. In spite of the relative simplicity of our model, the simulations remain quite formidable.

4.5 Results

Over the course of a 50 ps simulation, the lowest lying CIS excitation samples a variety of electronic configurations ranging from localized PCBM excitons to charge-separated and charge-transfer states with varying degrees of charge separation. In Figure 4.3, we show the lowest few CIS excitation energies following excitation at $t = 0$ fs to the lowest CIS state for one representative simulation. The labels refer to snap-shots taken at 50 fs intervals to visualize the various electronic configurations sampled by our approach in Figure 4.4. First, we note that following promotion to the lowest lying CIS at $t = 0$ there is very little energetic reorganization or relaxation compared to the overall thermal fluctuations that modulate the CIS eigenvalues. This can be rationalized since the excitation in the π^* orbitals at any given time is largely delocalized over one or more molecular units and hence the average electron-phonon coupling per C=C bond is quite small. The number of avoided crossings that occur between lowest lying states is highly striking, signaling that the internal molecular dynamics even at 100 K is sufficient to bring these states into regions of strong electronic coupling.

In Figure 4.5, we show a histogram of the energies of the lowest five CIS energies

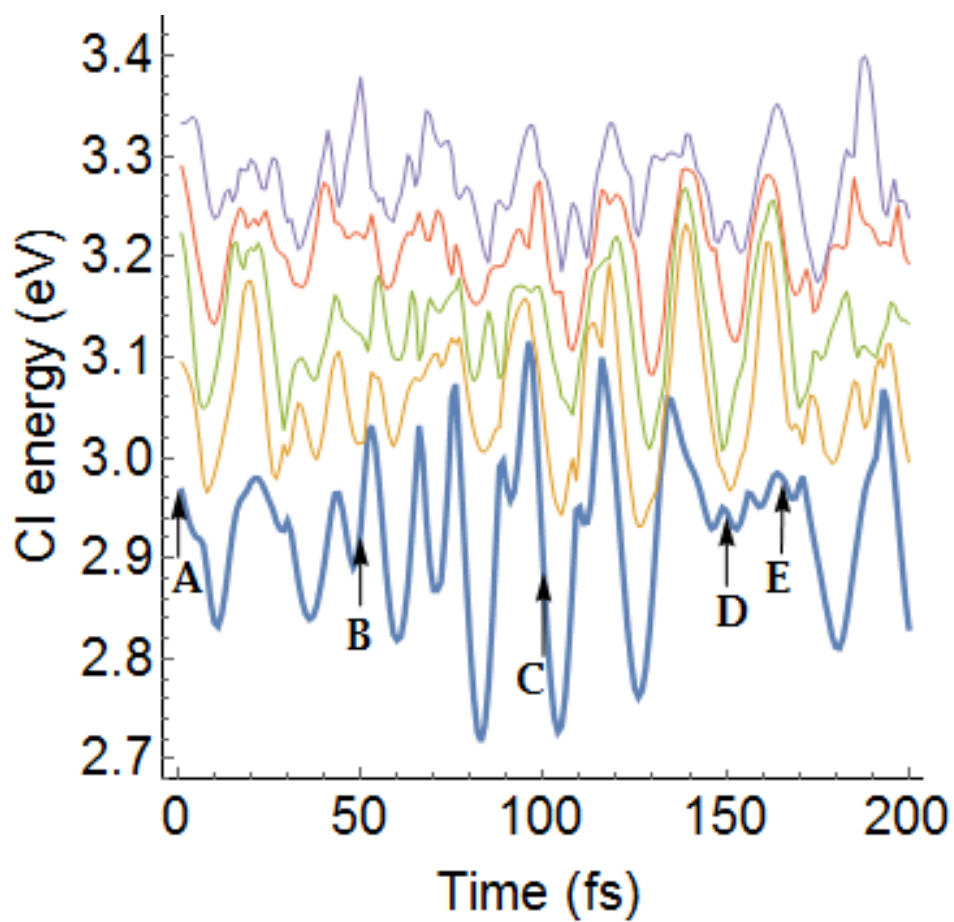


Figure 4.3: Single CI (CIS) energies for the first 200 fs following excitation to the lowest CIS state. Throughout the simulation, the lowest lying state (in blue) remained populated and varied in character from excitonic to charge-separated. Labels A-E refer to the configurations shown in Figure 4.4.

accumulated over 50 ps of simulation time following promotion to the lowest CIS state. Focusing upon the lowest lying state (in blue), fluctuations due to molecular dynamics can account for nearly 0.25 eV of inhomogeneous broadening of this state bringing it (and similarly for the other states) into regions of strong electronic coupling with nearby states which dramatically changes the overall electronic character of the state from purely charge-transfer to purely excitonic on a rapid time-scale.

We next consider the origins of the energy fluctuations evidenced in Figure 4.3. While we only show a 200 fs segment of a much longer 50 ps simulation, over this period one can see that the CI energies are modulated with a time-period of about 20 fs. Indeed, the Fourier transform of the average CI excitation energy reveals a series of peaks between 1400-1700 cm^{-1} which corresponds to the C=C stretching modes present in the polymer chains and fullerene molecules. We conclude that small-scale vibronic fluctuations in the molecular structures and orientations produce significant energetic overlap between different electronic configurations in organic polymer-fullerene heterojunction systems and speculate that this may be the origins of efficient charge separation in such systems.

A variety of states are produced by our model and we categorize them as excitonic (electron/hole on the same molecular unit) occupying $\approx 50\%$ of the states, charge-transfer (electron on PCMB/hole on PPV#1 (nearest to PCBM)) occupying $\approx 15\%$ of the states, or charge separated (electron on PCBM/hole on PPV #2 or #3) occupying $\approx 25\%$ of the states. These are shown in Fig. 4.6 where we indicate the local charge-density of each $\text{C}2p_z$ orbital by a blue (positive) or red (negative) sphere scaled in proportion to the local charge on each site.

In Figure 4.6 we show a sequences of snap shots taken every 50 fs following the initial excitation. These figures reveal the highly dynamical nature of the lowest lying excitation in which the system samples excitonic configurations (a), charge-transfer configurations (b,c), charge-separated states in which the electron and hole are separated by at least one polymer chain (d,e), and highly mixed charge-transfer/excitonic states as in (e,f). The scenario depicted here is not an exceptional case within our simulation. Here, the initial excited state is clearly localized on the PCBM unit with a high degree of excitonic character. There is clearly some charge separation within the PCBM; however, both the electron and hole clearly reside on the PCBM. After 50 fs (*c.f.* Figure 4.4), structural fluctuations in part induced by changes in electronic density and in part by the thermal fluctuations of the surrounding medium bring this state nearly into resonance with the second CIS state inducing charge separation between the PCBM and a nearby PPV oligomer. Further fluctuations bring this state into resonance with other charge separated states as shown in Figure 4.4 c, d, and f. Because our quantum subspace is restricted to the molecules shown in Figure 4.4, charge separation to more distant regions can not occur.

Figure 4.7 shows a histogram of the energy gaps between the first and higher-lying excited states of our system. According to our heuristic model, the mean (μ) and variance (σ^2) of the gap distributions can be used as input to estimate the state-to-state rate for this system under the mapping that $\mu = \Delta_o$ and $\sigma^2 = \overline{\delta V^2}$ as per Equation 4.3. Furthermore, we take $T_d^{-1} \approx \bar{V}/\hbar$ as an estimate of the decoherence time. The results are shown in Table. 4.1. The estimated transition rates are consistent with the observation that the system rapidly samples a wide number

of possible configurations over the course of the molecular dynamics simulation. On average, the state-to-state coupling of 70 meV is comparable to the average energy gaps between the lowest states. This brings the system into the regime of strong electronic coupling. However, larger couplings also imply *shorter* electronic decoherence times—which dramatically limit the the ability of charges to separate by tunneling. In this case, any superposition CI states resulting from the quantum mechanical time-evolution of the system would collapse to single eigenstate on a sub-10 fs time-scale due to the interaction with the vibronic degrees of freedom. Based upon our model and simulations, we estimate that within 20 fs, population in any low-lying electronic state is effectively mixed with nearby states simply due to the underlying vibrations of the lattice.

Fig. 4.6 illustrates how the electronic nature of the lowest lying excitation changes over a short time period. Shown here are the excess charge-densities at each atomic site taken at 1 fs intervals. At each 1 fs time-step, the electronic character changes wildly due to strong coupling between the electronic and vibrational degrees of freedom.

Table 4.1: Estimated interstate transition rates from Equation 4.20 and vibronic couplings.

Transition	Δ_o (eV)	\bar{V} (eV)	T_d (fs)	\bar{k}^{-1} (fs)
1 \rightarrow 2	0.11	0.06	11.41	21.8
1 \rightarrow 3	0.18	0.08	8.66	28.6
1 \rightarrow 4	0.26	0.08	8.70	50.0

4.6 Conclusions

We present here the results of hybrid quantum/classical simulations of the excited states of a model polymer/fullerene heterojunction interface. Our results indicate that dynamical fluctuations due to both the response of the system to the initial excitation and to thermal noise can rapidly change the character of the lowest lying excited states from purely excitonic to purely charge separated over a time scale on the order of 100 fs. In many cases, an exciton localised on the fullerene will dissociate into a charge-transfer state with the hole (or electron) delocalized over multiple polymer units before localizing to form a charge-separated state. While the finite size of our system prevents further dissociation of the charges, the results are clearly suggestive that such interstate crossing events driven by bond-fluctuations can efficiently separate charges to a distance where their Coulombic attraction is comparable to the thermal energy.

The nuclear motions most strongly coupled to the electronic degrees of freedom correspond to C=C bond stretching modes implying that small changes in the local lengths have a dramatic role in modulating the electronic couplings between excited states. Since $kT \ll \hbar\omega$ for these modes, they should be treated quantum mechanically rather than as classical motions. Generally speaking, including quantum zero-point effects into calculation of Fermi golden-rule rates leads to *slower* transition rates than those computed using classical correlation functions which implies that the values estimated here are the upper bounds for the actual transition rates. The results presented here corroborate recent ultrafast experimental evidence suggesting

that free polarons can form on ultrafast timescales (sub 100 fs) and underscore the dynamical nature of the bulk-heterojunction interface. [76, 77, 78]

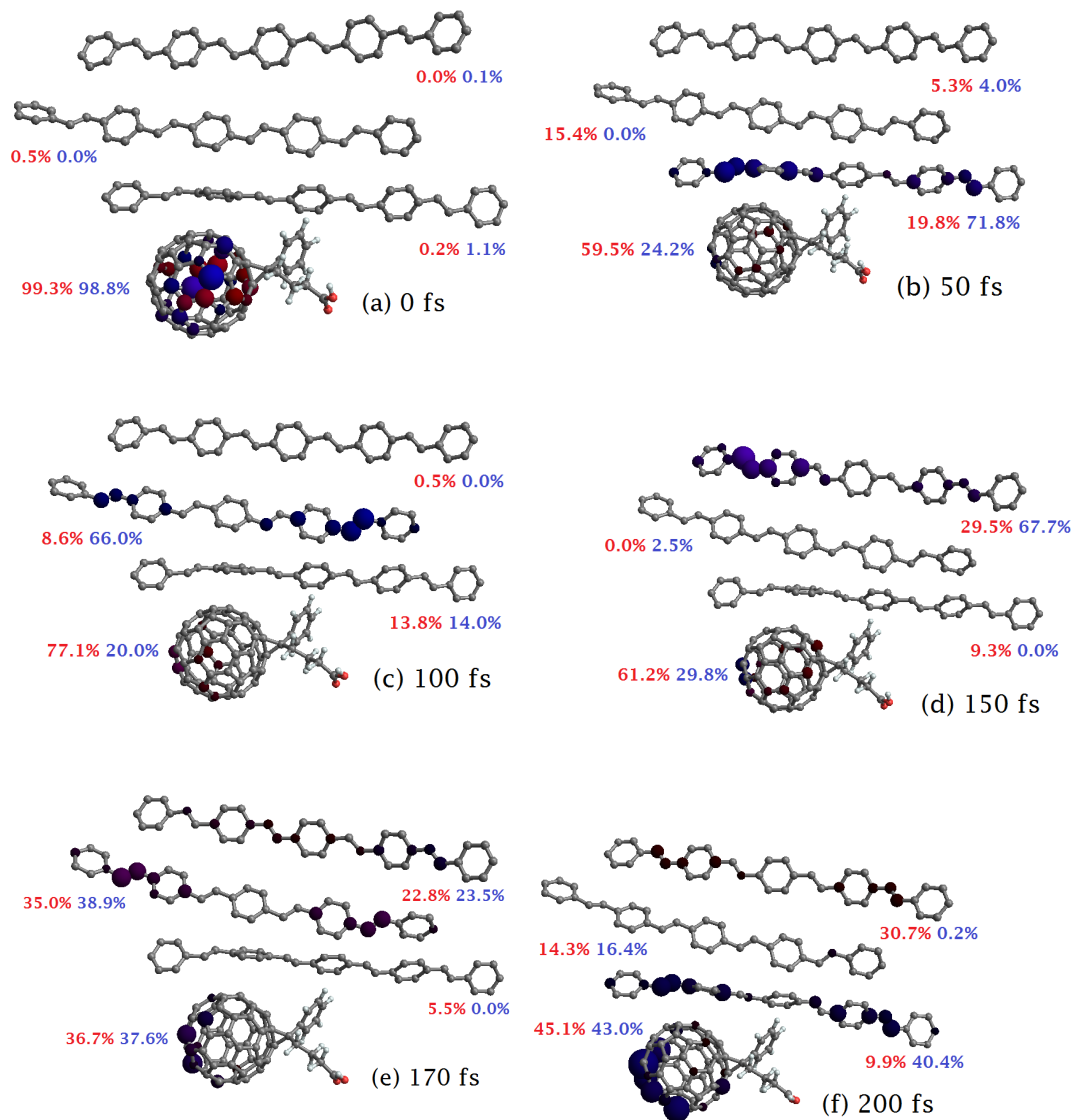


Figure 4.4: Sequence of states following initial excitation. In this particular simulation, the initial excited state population was localized on the PCBM. This population rapidly dissociates into charge-transfer and then charge-separated configurations within 100-150 fs. This scenario appears to be a ubiquitous feature of our simulations indicating that fluctuations alone can carry the system from a localized charge-transfer state to charge-separated states, eventually to current-producing polaron states.

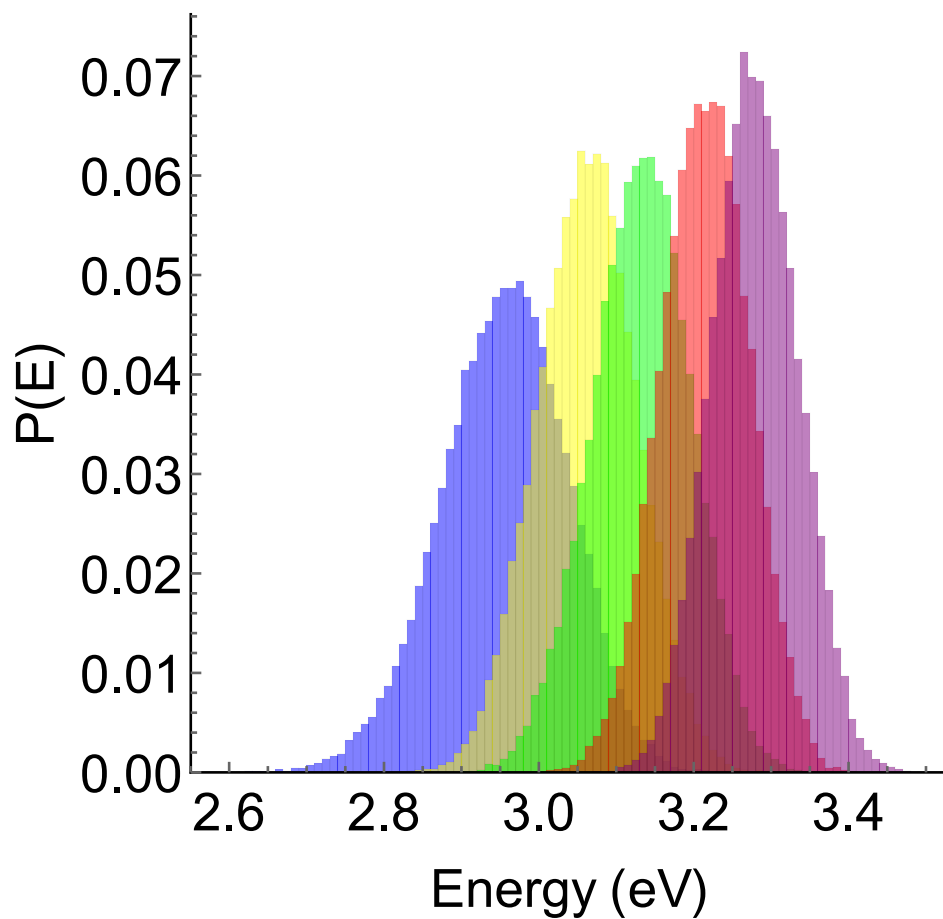


Figure 4.5: Histogram distribution of the five lowest excitation energy levels over a 50,000 ps simulation. Throughout the simulation, the lowest lying state (in blue) remained populated and varied in character from excitonic to charge-separated.

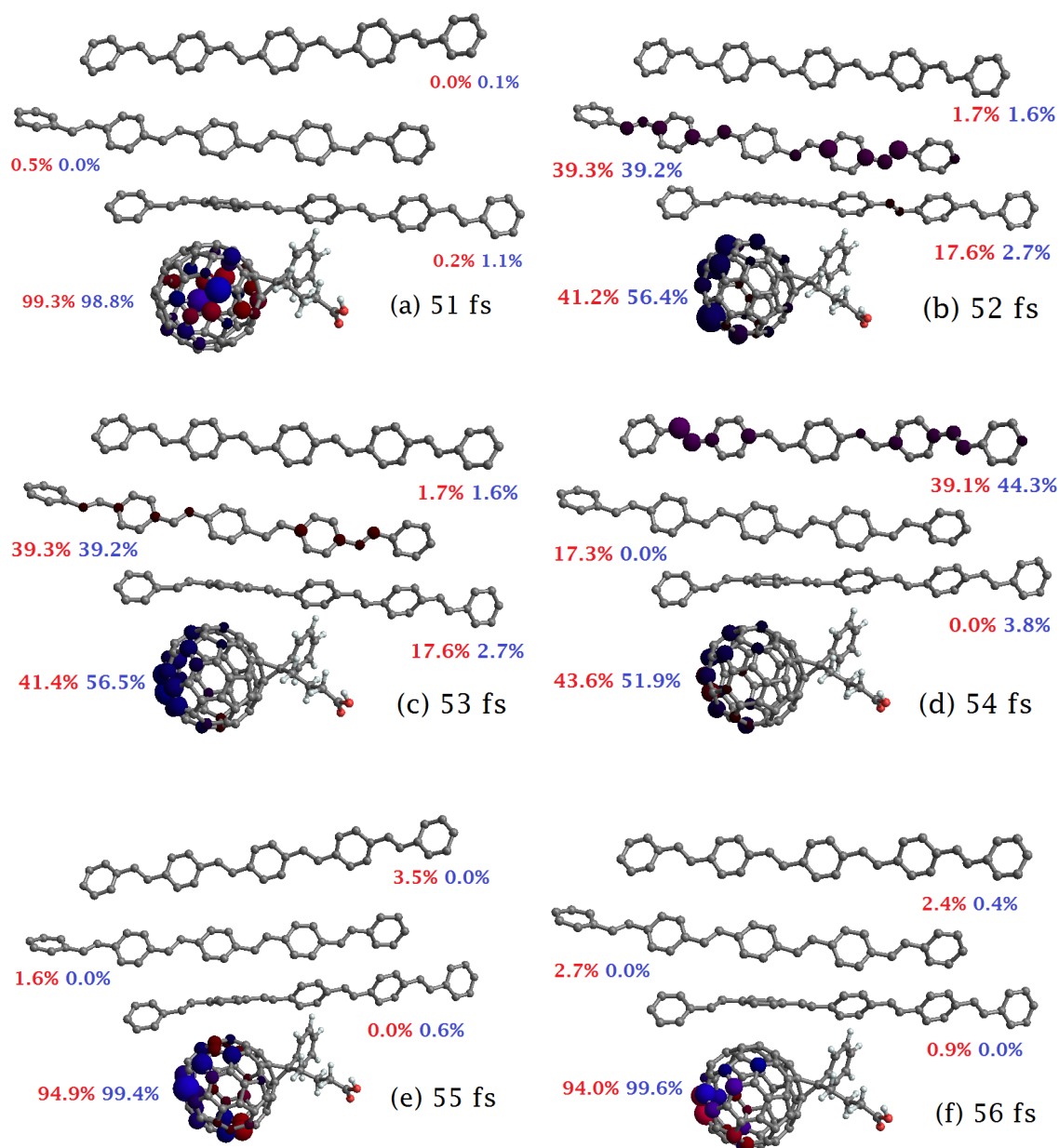


Figure 4.6: A 6 fs time history from 51 to 56 fs of the first excited CI state is shown in Figure 4.3. This series resides around an avoided crossing between the first and second excited state. Showing how a CT state at the interface can evolve into exciton states farther into the bulk around one avoided crossing point. After the excited states diverge, the exciton in the bulk collapses back into an exciton localized on the PCBM.

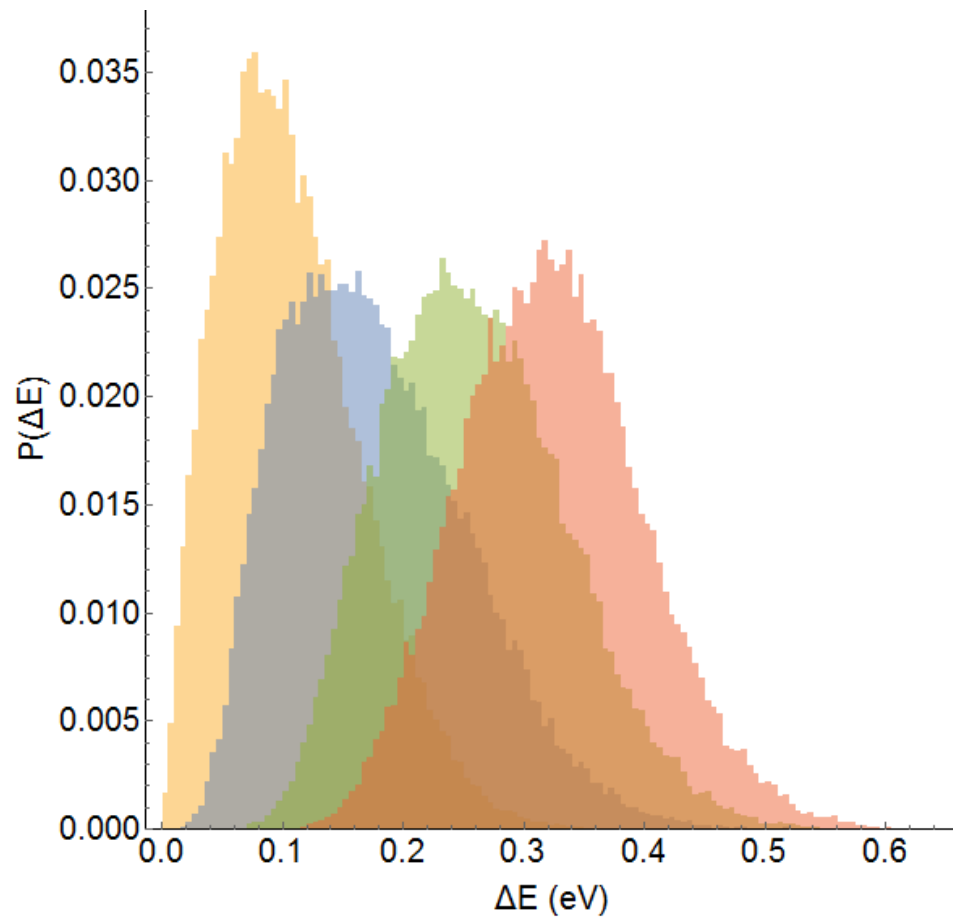


Figure 4.7: Histogram of energy gaps between the first excited and higher-lying excited states. Gold: $1 \rightarrow 2$, blue: $1 \rightarrow 3$, green: $1 \rightarrow 4$, and red: $1 \rightarrow 5$.

Chapter 5

Quantum simulations of charge-separation at a model donor-acceptor interface: role of delocalization and local packing

5.1 Introduction

Advances in both materials and device fabrication have lead to the development of highly efficient organic polymer-based photovoltaic cell (OPV) in which the power conversion efficiency is in excess of 10-11% under standard solar illumination [3] and efficiencies as high as 12% in multi-junction OPVs. This increase in power conversion

efficiency indicates that mobile charge carriers can be efficiently generated and collected in well-optimized devices; however, the underlying photo-physical mechanism for converting highly-bound molecular (Frenkel) excitons into mobile and asymptotically free photocarriers remains elusive in spite of vigorous, multidisciplinary research activity. [58, 59, 60]

The generic photophysical pathway that underlay the generation of mobile charge carriers in the OPV starts with an exciton being formed inside the system. The exciton dissociates at the interface into a charge transfer state with a small electron/hole separation. The charge transfer state is bound by Coulombic attraction to the interface, impeding the ability of the particles to migrate away from the interface to form free charge carriers. Ultrafast spectroscopic measurements on OPV systems have reported that charged photoexcitations are generated on ≤ 100 -fs [11, 16, 24, 25, 26, 27, 28] time-scales, despite the strong Coulombic attraction due to the low dielectric constant prevalent in OPV's. Experiments by Gelinias *et al.*, [10] in which Stark-effect signatures in transient absorption spectra were analysed to probe the local electric field as charge separation proceeds, indicate that electrons and holes separate by as much as 40 Å over the first 100 fs and evolve further on pico-second time scales to produce unbound and hence freely mobile charge pairs.

We recently presented a fully quantum dynamical model of photo-induced charge-fission at a polymeric type-II heterojunction interface. [40] Our model supposes that the energy level fluctuations due to bulk atomic motions create the resonant conditions for coherent separation of electrons and holes via long-range tunnelling. Simulations based upon lattice models reveal that such fluctuations lead to strong

quantum mechanical coupling between excitonic states produced near the interface and unbound electron/hole scattering states resulting in a strong enhancement of the decay rate of photo excitations into unbound polaronic states.

A microscopic model of the interface is required to understand the mechanisms that promote charge separation. This requires knowing the morphology and the finest details of the interface and its electronic structure. Currently *ab-initio* methods are unable to handle the size of the simulations required to properly simulate the heterojunction. We take a molecular mechanics/quantum mechanics (MM/QM) approach to studying Poly(p-phenylene vinylene) (PPV)/ Phenyl-C61-butyric acid methyl ester (PCBM) heterojunctions. We explore the effect that the positioning of the molecules at the interface has on the electronic properties and estimated rate constants of the systems. Polymer microstructural probes have revealed general relationships between disorder, aggregation, and electronic properties in polymeric semiconductors. The distribution of torsion angles for the PPV molecule at the interface are larger than in the bulk, adding to the structural disorder of the PPV molecules closest to the interface. Moreover, aggregation (ordering) can be perturbed by the blend-ratio and composition of the donor/acceptor polymers. [78]

5.2 Methods

Our simulations employ a modified version of the TINKER molecular dynamics (MD) package [50] in which the MM3 [70] intra-molecular bonding parameters were

allowed to vary with the local π -electronic density as described by a Parisier-Parr-Pople (PPP) semi-empirical Hamiltonian [71, 72, 79, 80]. Similar approaches have been described by Rossky [81] and Warshal [82] to include electronic dynamics into an otherwise classical force field description.

At each time-step of the simulation, we compute the Hartree-Fock (HF) ground state for the π system and use configuration interaction (singles) (CIS) to describe the lowest few $\pi \rightarrow \pi^*$ excitations. Intermolecular interactions within the active space are introduced via non-bonding Coulombic coupling terms and static dispersion interactions contained within the MM3 forcefield. All electronic excitations are confined to the π -active orbitals. We used a total of 10 occupied and 10 unoccupied Hartree Fock molecular orbitals to construct the electron/hole configurations for the CI calculations.

During the equilibration steps, we assume the system to be in its electronic ground state, after which we excite the system to the first CIS excited state and allow the system to respond to the change in the electronic density within the adiabatic Born-Oppenheimer approximation. It is important to note that the excited state we prepare is not the state which carries the most oscillator strength to the ground nor do we account for non-adiabatic surface hopping-type transitions in our approach. [75, 73, 74] The dynamics simulations shown reflect the longer-time fate of the lowest-lying excited state populations and sample possible configurations that can be accessed by the system. The combination of a classical MD forcefield with a semi-empirical description of a selected few molecules within the system seems to be a suitable compromise between a fully *ab initio* approach which would be limited to

only a few molecules and short simulation times and a fully classical MD description which would neglect any transient changes in the local electronic density. [26]

We specifically chose three separate clusters of molecules to represent model bulk-hetrojunctions in order to study how varying the blend and positioning of the molecules affect the penetration of extended intra molecular electronic states into the bulk region. In each case study, we selected a subgroup of PCBM molecules and PPV chains and treat the π -electrons in these units explicitly while the remaining molecules in the simulations were treated using the purely classical MM3 force-field. The number of π -active PCBM molecules varies between each simulation, allowing each system to have a different blend ratio inside the π -active system. The placement of PPV molecules vary in two of the simulations, changing the number of PPV molecules in direct contact with PCBM molecules, fundamentally changing the hetrojunction.

Figure 3.3 shows snapshots from the three cases studied. In each, the red and blue colored spheres represent atoms included in the quantum-chemical description. Each snapshot corresponds to a periodic simulation cell following equilibration at 100 K and 1 ATM pressure. The system has periodic boundary conditions in the X and Y directions. In Case A, we selected 2 interfacial PCBMs and 3 nearby π -active PPV oligomers that penetrate into the bulk polymer region, including a total of 230 carbon $2p_z$ orbitals. In Case B, we selected 3 PCBM and 3 nearby PPV oligomers expanding the π -active molecules that form the inter-facial hetrojunction, including a total of 288 $2p_z$ orbitals. The system has the same boundary conditions as case A and is set up such that the main difference is in the placement of the PPV oligomers. In

simulation C we selected 1 PCBM and 3 PPV oligomers that penetrate into the bulk using periodic boundary conditions and 172 carbon $2p_z$ orbitals. This simulation was set up to be very similar to case A, only adding a single PCBM molecule to the inter-facial region.

5.3 Results

Over the course of eight 10 ps simulations, the lowest lying CIS excitation samples a variety of electronic configurations ranging from localized excitons to charge-separated, charge-transfer and de-localized configurations. Figure 5.1 shows the electronic configurations with varying degrees of charge separation, their occupancy can be seen in Figure 5.2. We categorize the states into four types, (EX) represents the exciton configurations, characterized as having $>50\%$ of the electron/hole density on a single molecule. The exciton configuration occupies $\approx 58\%$ of the states for simulation A, $\approx 32\%$ for simulation B and $\approx 52\%$ for simulation C. (CT) represents the charge-transfer configurations, characterized as having $>50\%$ of the electron/hole density occupying adjacent molecules. The charge-transfer configuration occupies $\approx 14\%$ of the states for simulation A, $\approx 19\%$ for simulation B and $\approx 12\%$ for simulation C. (CS) represents the charge separated configurations, characterized as having $>50\%$ of the electron/hole density occupying a PCBM and a PPV separated by a single molecule. The charge separated configuration occupies $\approx 26\%$ for simulation A, $\approx 49\%$ for simulation B, and $\approx 26\%$ for simulation C. (DLOC) represents the de-localized configurations, characterized as having $<50\%$ of the electron/hole density

on a single PPV or PCBM molecule.

The energies of the lowest CIS state following excitation at $t = 0$ fs for simulation A and B are shown in Figure 5.3 (Top). After excitation at $t = 0$ there is very little reorganization or relaxation in all of the systems simulated. The simulations appear to cycle through many electronic configurations in a short period of time leaving the impression of a weak electron-phonon coupling. This can be rationalized as the electron/hole density often de-localize over multiple molecules and many conjugated C-C bonds. Another striking effect of the systems are the large number of avoided crossings that occur between the lowest lying states. There are small thermally activated fluctuations within the simulation that appear to drive the oscillatory nature of the CIS energies, showing that even at 100 K the thermal fluctuations possess sufficient energy to bring these states into regions of strong electronic coupling.

In Figure 5.3 (Bottom) we show a histogram of the 5 lowest CIS energies accumulated over 40 ps of simulation time following promotion to the lowest CIS state. The range and mean CI energy for the first two excited states (blue and yellow) in simulation A are 2.5-3.17 eV and 2.82-3.22 eV and 2.95 eV and 3.02 eV and in simulation B 2.69-3.19 eV and 3.00 eV and 3.05 eV. A mean band-gap of 0.07 eV and 0.05 eV between the first and second excited state allows a mechanism for the formation of a continuum of excited states that can easily be brought into strong electronic coupling by small fluctuations in the CI energy of the system. The small average band gap and rapid oscillatory nature of the CI energies facilitate the systems ability to rapidly sample a great many different electronic configurations over the course of the simulation.

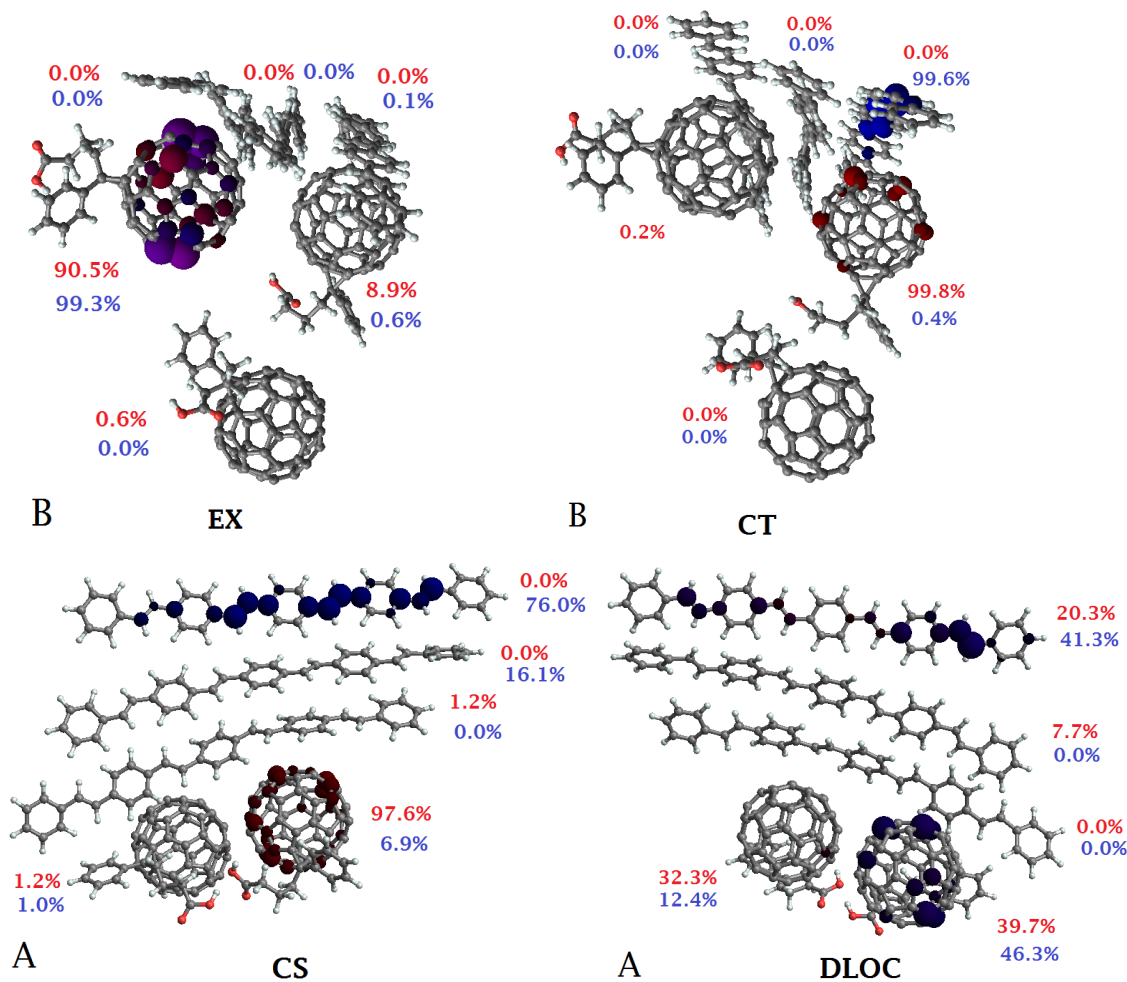


Figure 5.1: The dominant electronic configurations from simulation A (Bottom) and B (Top) as shown in Figure 3.3. The red and blue numbers denote the electron/hole density as a percent on the indicated molecule. The states correspond to the x axis in Figure 5.2. The four snapshots shown represent typical configurations for our systems. The top pictures from left to right present an exciton located on the PCBM molecule and a charge transfer configuration. The bottom pictures from left to right show a charge separated configuration and a partly de-localized configuration.

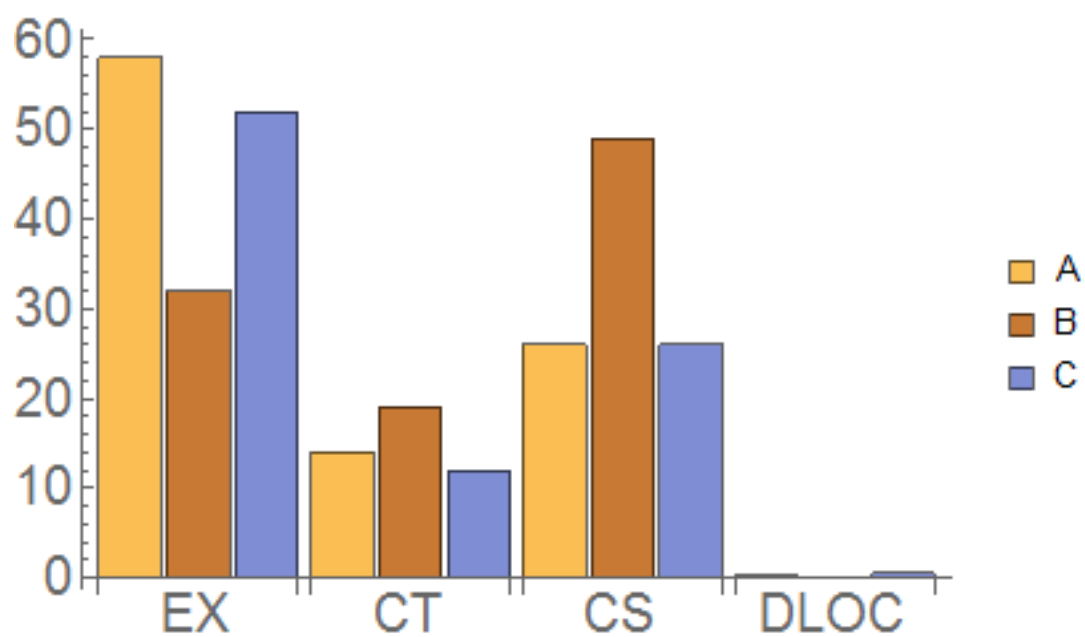


Figure 5.2: Histogram plot of the occupancy of the electronic configurations in system A, B and C taken every fs. Each cluster represents a different classification of the electronic configuration as shown in Figure 5.1.

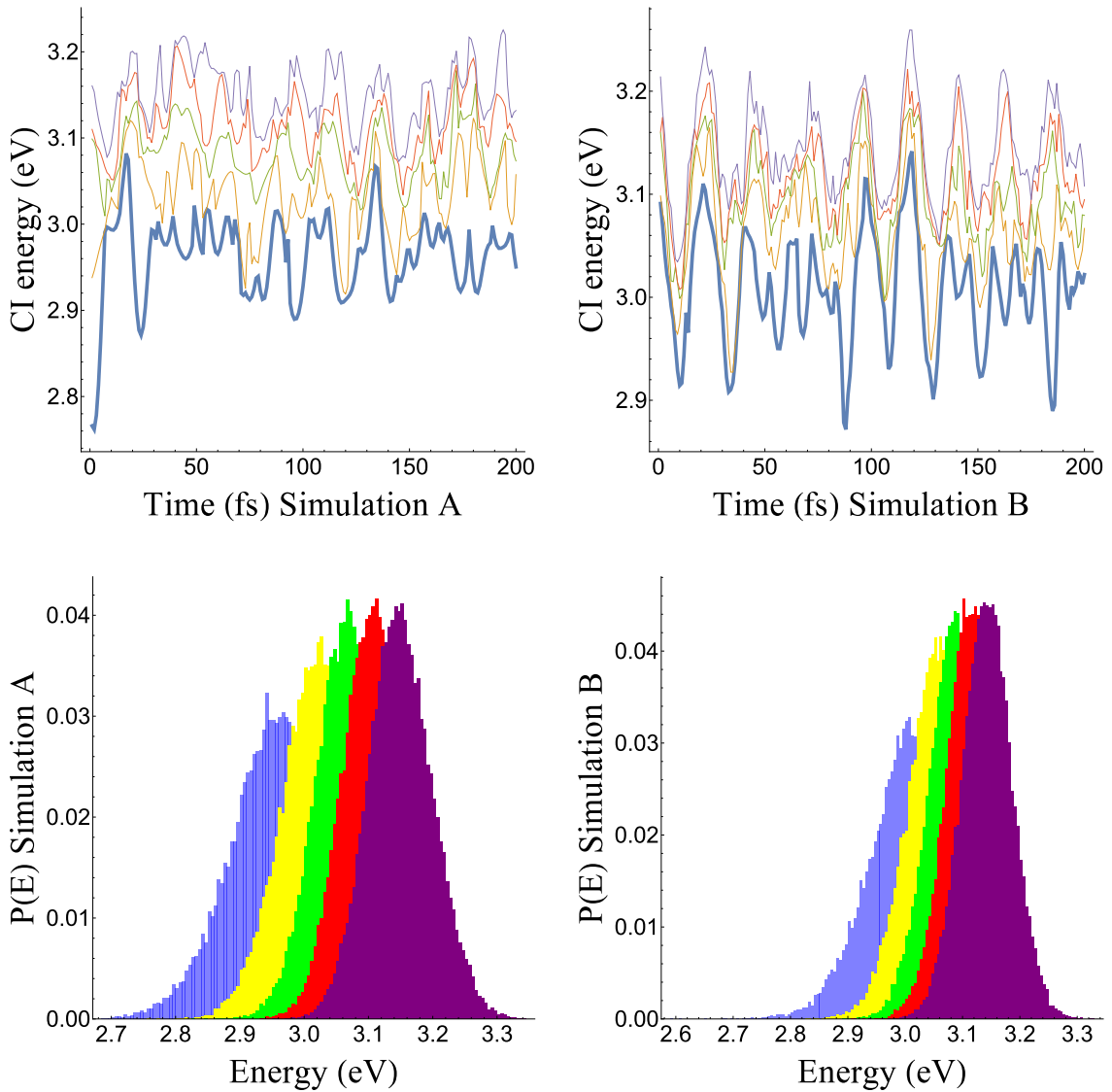


Figure 5.3: (Top) Single CI (SCI) energies for simulation A and B for the first 200 fs following excitation to the lowest SCI state. (Bottom) Histogram distributions of the 5 lowest excitation energy levels over a 200 ps simulation. Throughout the simulation, the lowest lying state (in blue) remained populated and varied in character from excitonic to charge-separated.

We next consider the origins of the energy fluctuations evidenced in Figure 5.3 (top). While we only show two 200 fs segments of eight 10 ps simulations over this period, one can see that the CI energies are modulated and cover a small range. Assuming that fluctuations due to the molecular dynamics can account for nearly 0.25 eV and the large number of avoided crossings present, due to the non-adiabatic nature of the simulations, allows the systems to come into strong coupling regimes. We conclude that small-scale vibronic fluctuations in the molecular structures and orientations produce significant energetic overlap between different electronic configurations to drive the system from purely excitonic to purely charge-transfer on a rapid time-scale.

Figure 5.4 shows the IR active modes that contribute to the modulation of the CI energies inside of each systems. The modulation of the CI energy appears to be heavily dependent upon the torsion and C=C stretching modes. The progression of the CI energies in time show that small fluctuations in these modes can easily bring the excited states into strong coupling regimes. This is evidenced by the prevalence of avoided crossings, making conclusions about the long term fate of the systems state difficult to predict. In each of the plots three distinct regions can be seen, the low frequency torsional modes occur between 200 and 500 cm^{-1} , the C=C stretching modes occur between 1300 and 1800 cm^{-1} and the C-H stretching modes occur between 2800 and 3300 cm^{-1} . The role of these thermal activated modes on the separation dynamics of excitons is still not entirely clear, yet warrant further investigation.

According to the model introduced in section 4.2 and 4.3 the mean (Δ_0) and

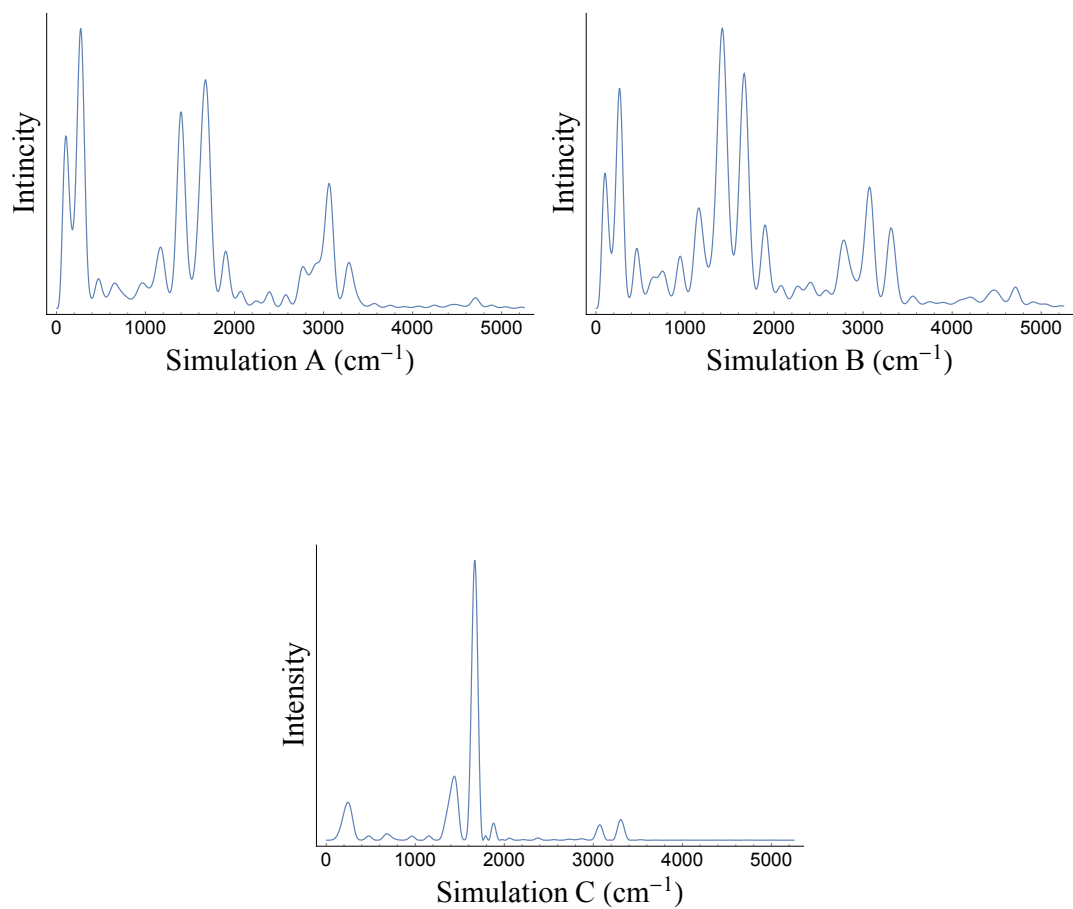


Figure 5.4: These plots show the active IR active modes that contribute to the modulation in the CI energies of the systems. Three distinct regions are visible in each plot. The low frequency torsional modes occur between 200 and 500 cm^{-1} , the C=C stretching modes occur between 1300 and 1800 cm^{-1} and the C-H stretching modes occur between 2800 and 3300 cm^{-1}

variance (\bar{V}) of the energy gap distributions shown in Figure 5.3 can be used as input to estimate the state to state transition rate for a two-level system. We take $T_d^{-1} \approx \bar{V}/\hbar$ as an estimate of the decoherence time and we introduce τ as the natural lifetimes of each state. The results are shown in Table 5.1. The estimated transition rates are consistent with the observations that the systems rapidly sample a wide number of possible configurations over the course of the molecular dynamics simulation. On average, the state to state couplings of 56 meV for simulation A and 48 meV for simulation B are comparable to the average energy gaps between the lowest excited states. The strong electronic coupling allows for rapid transitions; however, larger couplings also imply shorter electronic decoherence times, effectively quenching the ability of charges to separate by tunnelling.

Table 5.1: Estimated interstate transition rates and vibronic couplings for simulation A, B and C.

Transition	Δ_o (eV)	$\langle V \rangle$ (eV)	T_d (fs)	k^{-1} (fs)
A				
1→2	0.070	0.050	13.16	19.5
1→3	0.12	0.056	11.75	32.9
1→4	0.16	0.063	10.45	38.9
B				
1→2	0.050	0.042	15.67	18.9
1→3	0.09	0.049	13.43	29.3
1→4	0.12	0.052	12.66	40.0
C				
1→2	0.11	0.057	11.41	21.8
1→3	0.18	0.076	8.66	28.6
1→4	0.26	0.076	8.70	50.0

5.4 Conclusions

We present here the results of hybrid QM/MM simulations of the excited states of model PPV/PCBM heterojunction interfaces. Our results indicate that varying the blend ratio and placement of the molecules comprising the heterojunction greatly affect the distribution of states yet have little effect upon the rate constants of the system. We also propose that thermal noise can rapidly change the character of the lowest lying excited state from purely excitonic to charge separated on a time scale of sub 100 fs.

Simulations A and C have a very similar placement of molecules, only differing in that simulation A adds a PCBM molecule to the heterojunction. The addition of the PCBM only slightly changes the distribution of states as seen in Figure 5.3. The exciton states continue to be the most favored state inside the system, even slightly increasing in probability, while the delocalized states slightly decrease in probability. Simulation B completely changes the heterojunction, placing three PPV and two PCBM molecules at the interface as seen in Figure 3.3. The states generated by simulation B are radically different from those seen in simulation A and C as seen in Figure 5.3. The probability of finding the system in the exciton state is dramatically reduced while the charge separated state becomes predominant. This result is quite interesting as it highlights that the complexity of simulating heterojunctions resides not only in the size of the system but on how the donor/accepter interface is chosen.

All three systems start with an exciton localized on the PCBM and dissociating into a charge transfer state with the hole (or electron) delocalized over multiple

polymer units before localizing to form charge separated states. There are a wide range of electronic states tightly clustered within a small energy band, allowing small changes in local bond lengths to have a dramatic role in modulating the electronic couplings between excited states. We speculate that the dramatic shift in population seen in simulation B can be caused by disorder in the PPV molecules reducing the band gap by 20 meV. The PPV molecules comprising the interface region undergo large distortions in the C-C torsion angles allowing the molecules to cycle through a larger range of configurations inside of a short time interval. The vibrational modes that couple the strongest to the electronic degrees of freedom correspond to the low frequency out of plane torsion mode at (219cm^{-1}) [83]. The presence of more π -active PPV molecules at the interface also appear to lead to more avoided crossing regions and the ability of the system to more efficiently dissociate excitons into charge transfer and charge separated states to a distance to where their Coulombic attraction is comparable to the thermal energy. While the finite size of our system prevents further dissociation of the charges, the results are suggestive that such interstate crossing events driven by bond-fluctuations can efficiently separate the charges. The results presented here corroborate recent ultra fast experimental evidence suggesting that free polarons can form on ultra fast time scales (sub 100 fs) and that thermally activated low-frequency torsional modes are key in effective electron-hole separation in PPV/PCBM heterojunctions.

Bibliography

- [1] A. G. MacDiarmid C. K. Chaing H. Shirakawa, E. J. Louis and A. J. Heeger. Synthesis of electrically conducting organic polymers: Halogen derivatives of polyacetylene. *Chemical. Communications*, 16:578–580, 1977.
- [2] C. Zhang V. I. Srdanov A. J. Heeger G. Stucky N. S. Sariciftci, D. Braum and F. Wudl. Semiconducting polymer-buckminsterfullerene heterojunctions: Diodes, photodiodes, and photovoltaic cells. *Applied Physics Letters*, 62:585–587, 1993.
- [3] Zhicai He, Chengmei Zhong, Shijian Su, Miao Xu, Hongbin Wu, and Yong Cao. Enhanced power-conversion efficiency in polymer solar cells using an inverted device structure. *Nature Photonics*, 6(9):591–595, 2012.
- [4] National Renewable Energy Laboratory. Research cell efficiency records. Sep 25, 2016.
- [5] W. Shockley and H. J. Queisser. Detailed Balance Limit of Efficiency of p-n Junction Solar Cells. *Journal of Applied Physics* , 32:510-519, 1961.
- [6] D Beljonne, E Hennebicq, C Daniel, L M Herz, C Silva, G D Scholes, F J M Hoeben, P Jonkheijm, A P H J Schenning, S C J Meskers, R T Phillips, R H Friend, and E W Meijer. Excitation migration along oligophenylenevinylene-based chiral stacks: delocalization effects on transport dynamics. *Journal of Physical Chemistry B*, 109(21):10594–10604, 2005.
- [7] Elisabetta Collini and Gregory D. Scholes. Coherent intrachain energy migration in a conjugated polymer at room temperature. *Science*, 323(5912):369–373, 2009.
- [8] Gregory S. Engel, Tessa R. Calhoun, Elizabeth L. Read, Tae-Kyu Ahn, Tomas Mancal, Yuan-Chung Cheng, Robert E. Blankenship, and Graham R. Fleming.

- Evidence for wavelike energy transfer through quantum coherence in photosynthetic systems. *Nature*, 446(7137):782–786, 2007.
- [9] Yongqian Gao, Thomas P. Martin, Edwards T. Niles, Adam J. Wise, Alan K. Thomas, and John K. Grey. Understanding morphology-dependent polymer aggregation properties and photocurrent generation in polythiophene/fullerene solar cells of variable compositions. *Journal of Physical Chemistry C*, 114(35):15121–15128, 2010.
- [10] Simon Gélinas, Akshay Rao, Abhishek Kumar, Samuel L. Smith, Alex W. Chin, Jenny Clark, Thomas S. van der Poll, Guillermo C. Bazan, and Richard H. Friend. Coherent charge separation in organic semiconductor photovoltaic diodes. *Science*, 343:512–516, 2014.
- [11] G. Grancini, M. Maiuri, D. Fazzi, A. Petrozza, H-J. Egelhaaf, D. Brida, G. Cerullo, and G. Lanzani. Hot exciton dissociation in polymer solar cells. *Nature Materials*, 12(1):29–33, 2013.
- [12] Loren G. Kaake, Daniel Moses, and Alan J. Heeger. Coherence and uncertainty in nanostructured organic photovoltaics. *Journal of Physical Chemistry Letters*, 4(14):2264–2268, 2013.
- [13] Nicholas R. Monahan, Kristopher W. Williams, Bharat Kumar, Colin Nuckolls, and X.-Y. Zhu. Direct observation of entropy-driven electron-hole pair separation at an organic semiconductor interface. *Physical Review Letters*, 114:247003, 2015.
- [14] Shaul Mukamel. Comment on "coherence and uncertainty in nanostructured organic photovoltaics". *Journal of Physical Chemistry A*, 117:10563–10564, 2013.
- [15] Franoise Provencher, Nicolas Berube, Anthony W. Parker, Gregory M. Greetham, Michael Towrie, Christoph Hellmann, Michel Cote, Natalie Stingelin, Carlos Silva, and Sophia C. Hayes. Direct observation of ultrafast long-range charge separation at polymer–fullerene heterojunctions. *Nature Communications*, 5:4288, 2014.
- [16] C-X Sheng, T Basel, B Pandit, and Zeev Vally Vardeny. Photoexcitation dynamics in polythiophene/fullerene blends for photovoltaic applications. *Organic Electronics*, 13(6):1031–1037, 2012.
- [17] Hiroyuki Tamura, Eric R. Bittner, and Irene Burghardt. Exciton dissociation at donor-acceptor polymer heterojunctions: Quantum nonadiabatic dynamics and effective-mode analysis. *Journal of Chemical Physics*, 126(2):021103, 2007.

- [18] Hiroyuki Tamura and Irene Burghardt. Ultrafast charge separation in organic photovoltaics enhanced by charge delocalization and vibronically hot exciton dissociation. *Journal of the American Chemical Society*, 135(44):16364–16367, 2013.
- [19] X. N. Yang J. Loos C. W. T. Bulle-Lieuwma A. B. Sieval J. C. Hummelen R. A. J. Janssen Van Duren, J. K. J. Relating the morphology of poly(p-phenylene vinylene)/methanofullerene blends to solar-cell performance. *Advanced Functional Materials*, 14:425, 2004.
- [20] M. W. P. Blom C. Melzer B. de Boer J. K. J. Van Duren R. A. J. Janssen V. D. Mihailetschi, L. J. A. Kroster. Compositional dependence of the performance of poly(p-phenylene vinylene):methanofullerene bulk-heterojunction solar cells. *Advanced Functional Materials*, 15:795, 2005.
- [21] Koen Vandewal Felix P. V. Koch Natalie Stingelin Paul Smith Michael F. Toney Alberto Salleo Rodrigo Noriega, Jonathan Rivnay. A general relationship between disorder, aggregation and charge transport in conjugated polymers. *Nature Materials*, pages 1038–1044, 2013.
- [22] Martina Causa, Jelissa De Jonghe-Risse, Mariateresa Scarongella, Jan C. Brauer, Ester Buchaca-Domingo, Jacques-E. Moser, Natalie Stingelin and Natalie Banerji. The fate of electron-hole pairs in polymer:fullerene blends of organic photovoltaics. *Nature Communications*, 7:12556, 2016.
- [23] Ryan D. Pensack, Changhe Guo, Kiarash Vakhshouri, Enrique D. Gomez, and John B. Asbury. Influence of Acceptor Structure on Barriers to charge Separation in Organic Photovoltaic Materials. *Journal of Physical Chemistry C*, 116:4824–4831, 2012.
- [24] Natalie Banerji. Sub-picosecond delocalization in the excited state of conjugated homopolymers and donor–acceptor copolymers. *Journal of Material Chemistry C*, 1(18):3052, 2013.
- [25] Natalie Banerji, Sarah Cowan, Mario Leclerc, Eric Vauthey, and Alan J. Heeger. Exciton Formation, Relaxation, and Decay in PCDTBT. *Journal of the American Chemical Society*, 132(49):17459–17470, 2010.
- [26] Askat E. Jailaubekov, Adam P. Willard, John R. Tritsch, Wai-Lun Chan, Na Sai, Raluca Gearba, Loren G. Kaake, Kenrick J. Williams, Kevin Leung, Peter J. Rossky, and X-Y. Zhu. Hot charge-transfer excitons set the time limit for charge separation at donor/acceptor interfaces in organic photovoltaics. *Nature Materials*, 12(1):66–73, 2013.

- [27] NS Sariciftci and AJ Heeger. Reversible, Metastable, Ultrafast Photoinduced Electron-Transfer from Semiconducting Polymers to Buckminsterfullerene and in the Corresponding Donor-Acceptor Heterojunctions. *International Journal of Modern Physics B*, 8(3):237–274, 1994.
- [28] M Tong, N Coates, Daniel Moses, Alan J Heeger, Serge Beaupré, and M Leclerc. Charge carrier photogeneration and decay dynamics in the poly(2,7-carbazole) copolymer PCDTBT and in bulk heterojunction composites with PC₇₀BM. *Physical Review B*, 81(12):125210, 2010.
- [29] PF Barbara, TJ Meyer, and MA Ratner. Contemporary issues in electron transfer research. *Journal of Physical Chemistry*, 100(31):13148–13168, 1996.
- [30] Huckel. Approximation methods. *Applied Physics Letters*, 70:279, 1931.
- [31] A. Warshel and M. Levitt. Theoretical Studies of Enzymic Reactions: Dielectric, Electrostatic and Steric Stabilization of the Carbonium Ion in the Reaction of Lysozyme. *Journal of Molecular Biology*, 103:227–249, 1976.
- [32] N. Colin Baird and Michael J. S. Dewar. Ground State of Bonded Molecules the MINDO Method and Its Application to Hydrocarbons. *Journal of Chemical Physics*, 50:1262–1274, 1968.
- [33] Kimio Ohno. Some Remarks on the Pariser-Parr-Pople Method. *Theoretical Chemistry Accounts*, 2:219-227, 1964.
- [34] Harald Hoppe and Niyazi Serdar Sariciftci. Morphology of polymer/fullerene bulk heterojunction solar cells. *Journal of Material Chemistry*, 16:45–61, 2006.
- [35] A. Baumann, J. Lorrmann, C. Deibel, and V. Dyakonov. Bipolar Charge Transport in Poly(3-hexyl thiophene)/Methanofullerene Blends: A Ratio Dependent Study. *Condensed Matter*, 1–4, 2008.
- [36] Nesrin Tore, Elif Alturk Parlak, Ozlem Usluer, Daniel A. M. Egbe, Sait. E. San, Pelin Aydogan. Effect of blend ratio on poly(p-phenylene-ethynylene)-alt-poly(p-phenylene-vinylene) polymer solar cell. *Solar Materials*, 104:39–44, 2012.
- [37] M. R. Merad Boudia, A. Cheknane, B. Benyoucef, A. M. Ferouani and H. S. Hilal. Recent Modeling of MDMO-PPV: PCBM Solar Cells Versus Mixture Ratio, Electric Field and Incidence Angle with Hopping Model. *Evolving Trends in Engineering Technology*, 3:30–36, 2014.

- [38] Improvement in photovoltaic performance of anthracene-containing PPE-PPV polymer-based bulk heterojunction solar cells with silver nanoparticles. Nesrin Tore, Elif Alturk Parlak, Tulay Asli Tumay, Pelin Kavak, Serife Sarioglan, Sinem Bozar, Serap Gunes. *Journal of Nanoparticle Research*, 16:2297–2298, 2014.
- [39] Wojciech J. Grzegorzczak, Tom J. Savenije, Tienieke E. Dykstra, Jorge Piris, Juleon M. Schins, and Laurens D.A. Siebbeles. Temperature-Independent Charge Carrier Photogeneration in P3HT-PCBM Blends with Different Morphology. *Journal of Physical Chemistry C.*, 114:5182-5186, 2010.
- [40] Eric R. Bittner and Carlos Silva. Noise-induced quantum coherence drives photo-carrier generation dynamics at polymeric semiconductor heterojunctions. *Nature Communications*, 5:3119, 2014.
- [41] Carlos Silva. Organic photovoltaics: Some like it hot. *Nature Materials*, 5–6, 2012.
- [42] Carsten Deibel and Thomas Strobel. Origin of the Efficient Polaron-Pair Dissociation in Polymer-Fullerene Blends. *Physical Review Letters*, 103:1-4, 2009.
- [43] Charles L. Braun. Electric field assisted dissociation of charge transfer states as a mechanism of photocarrier production. *Journal of Chemical Physics*, 80:1984.
- [44] Jiye Lee, Koen Vandewal, Shane R. Yost, Matthias E. Bahlke, Ludwig Goris, Marc A. Baldo, Jean V. Manca, and Troy Van Voorhis. Charge Transfer State Versus Hot Exciton Dissociation in Polymer-Fullerene Blended Solar Cells. *Journal of the American Chemical Society*, 132:11878–11880, 2010.
- [45] Ignacio Franco and Sergei Tretiak. Electron-Vibrational Dynamics of Photoexcited Polyfluorenes. *Journal of the American Chemical Society*, 126:12130–12140, 2004.
- [46] Sharon E. Koh, Chad Risko, Demetrio A. da Silva Filho, Ohyun Kwon, Antonio Facchetti, Jean-Luc Bredas, Tobin J. Marks, and Mark A. Ratner. Modeling Electron and Hole Transport in Fluoroarene-Oligothiophene Semiconductors: Investigation of Geometric and Electronic Structure Properties. *Advanced Functional Materials*, 18:332-340, 2008.
- [47] Stijn Verlaak, David Beljonne, David Cheyns, Cedric Rolin, Mathieu Linares, Frederic Castet, Jerome Cornil, and Paul Heremans. Electronic Structure and

- Geminate Pair Energetics at Organic-Organic Interfaces: The Case of Pentacene/C60 Heterojunctions. *Advanced Functional Materials*, 19:3809–3814, 2009.
- [48] William Barford, Eric R. Bittner, and Alec Ward. Exciton Dynamics in Disordered Poly(p-phenylenevinylene). 2. Exciton Diffusion. *Journal of Physical Chemistry A*, 116:10319–10327, 2012.
- [49] David P. McMahon, David L. Cheung, and Alessandro Troisi. Why Holes and Electrons Separate So Well in Polymer/Fullerene Photovoltaic Cells. *Journal of Physical Chemistry Letters*, 2:2737–2741, 2011.
- [50] Jay W. Ponder. *TINKER: Software Tools for Molecular Design*, 4.2 ed, 2004.
- [51] Donald H. Lo and M. A. Whitehead. Accurate heats of atomization and accurate bond lengths. In Benzenoid hydrocarbons. *Canadian Journal of Chemistry*, 46:2027-2040, 1967.
- [52] Donald H. Lo and M. A. Whitehead. Molecular Geometry and Bond Energy. III. Cyclooctatetraene and Related Compounds. *Journal of the American Chemistry Society*, 91:238-242, 1969.
- [53] Attila Szabo, Neil S. Ostlund. *Modern Quantum Chemistry*. Dover., 1982.
- [54] J. W. Linnett. The force constants of some carbon-carbon bonds. *Transactions of the Faraday Society*, 37:469-473, 1941.
- [55] C. W. Tang. Two-Layer organic photovoltaic cell. *Applied Physics Letters* , 48:183–185, 1986.
- [56] U. Bach, D. Lupo, P. Comte, J. E. Moser, F. Weissortel, J. Salbeck, H. Spreitzer, and M. Gratzel. Solid-state dye-sensitized mesoporous TiO₂ solar cells with high photon-to-electron conversion efficiencies. *Nature* , 395:583–585, 1998.
- [57] M. Granstrom, K. Petritsch, A. C. Arias, A. Lux, M. R. Andersson, and R. H. Friend. Laminated fabrication of polymeric photovoltaic diodes. *Nature* , 395:257–260, 1998.
- [58] Hiroyuki Tamura, John G. S. Ramon, Eric R. Bittner, and Irene Burghardt. Phonon-driven ultrafast exciton dissociation at donor-acceptor polymer heterojunctions. *Physical Review Letters*, 100(10):107402, 2008.
- [59] Alessandro Troisi. How quasi-free holes and electrons are generated in organic photovoltaic interfaces. *Faraday Discussions*, 163:377–392, 2013.

- [60] Xiujuan Yang, Tienke E. Dykstra, and Gregory D. Scholes. Photon-echo studies of collective absorption and dynamic localization of excitation in conjugated polymers and oligomers. *Physical Review B*, 71:045203, 2005.
- [61] J. D. Zimmerman, X. Xiao, C. K. Renshaw, S. Wang, V.V. Diev, M. E. Thompson and S. R. Forrest. Independent Control of Bulk and Interfacial Morphologies of Small Molecular Weight Organic Heterojunction Solar Cells. *Nano Letters*, 12:4366–4371, 2012.
- [62] Peter Peumans, Stephen R. Forrest. Separation of geminate charge-pairs at donor-acceptor interfaces in disordered solids. *Chemical Physics Letters*, 398:27–31, 2004.
- [63] Karl Jug. Theoretical Basis and Design of the PPP Hamiltonian. *International Journal of Quantum Chemistry*, 37:403-414, 1990.
- [64] A. A. Baukulin, A. Rao, V. G. Pavelyev, P. H. M. van Loosdrecht, M. S. Pshenichnikov, D. Niedzialek, J. Cornil, D. Beljonne and R. H. Friend. The role of driving energy and delocalized States for charge separation in organic semiconductors. *Science*, 335:1340-1344, 2012.
- [65] Y. T. Fu, D. da Silva Filho, G. Sini, A. Asiri, S. Aziz, C. Risko and J. L. Bredas. Structure and Disorder in SquaraineC60 Organic Solar Cells: A Theoretical Description of Molecular Packing and Electronic Coupling at the Donor-Acceptor Interface. *Advanced Functional Materials*, 24:3790-3798, 2014.
- [66] Bittner R. Eric and Kelley C. Allen. The role of structural fluctuations and environmental noise in the electron/hole separation kinetics at organic polymer bulk-heterojunction interfaces. *Physical Chemistry Chemical Physics*, 17:28853, 2015.
- [67] H. Haken and G. Strobl. An exactly solvable model for coherent and incoherent exciton motion. *Zeitschrift für Physik*, 262:135–148, 1973.
- [68] Eric R. Bittner. Quantum Dynamics Applications in Biological and Materials Systems. *CRC Press.*, 2010.
- [69] Pengyu Ren and Jay W. Ponder. Polarizable Atomic Multipole Water Model for Molecular Mechanics Simulation. *Journal Physical Chemistry B.*, 107:5933-5947, 2003.
- [70] Norman L. Allinger, Fanbing Li, Liqun Yan, and Julia C. Tai. Molecular mechanics (mm3) calculations on conjugated hydrocarbons. *Journal of Computational Chemistry*, 11(7):868–895, 1990.

- [71] Rudolph Pariser and Robert G. Parr. A semi-empirical theory of the electronic spectra and electronic structure of complex unsaturated molecules. ii. *Journal of Chemical Physics*, 21(5):767–776, 1953.
- [72] John A. Pople. Electron interaction in unsaturated hydrocarbons. *Transactions of the Faraday Society*, 49(5):1375–1385, 1953.
- [73] John C. Tully. Molecular dynamics with electronic transitions. *Journal of Chemical Physics*, 93(2):1061–1071, 1990.
- [74] John C. Tully and Richard K. Preston. Trajectory surface hopping approach to nonadiabatic molecular collisions: The reaction of H^+ with D_2 . *Journal of Chemical Physics*, 55(2):562–572, 1971.
- [75] Giovanni Granucci and Maurizio Persico. Critical appraisal of the fewest switches algorithm for surface hopping. *Journal of Chemical Physics*, 126(13):134114, 2007.
- [76] A. W. Chin, J. Prior, R. Rosenbach, F. Caycedo-Soler, S. F. Huelga and M. B. Plenio. The role of non-equilibrium vibrational structures in electronic coherence and recoherence in pigmentprotein complexes. *Nature Physics*, 9:113-118, 2013.
- [77] C. Andrea Rozzi, S. Maria Falke, N. Spallanzani, A. Rubio, E. Molinari, D. Brida, M. Maiuri, G. Cerullo, H. Schramm, J. Christoffers and C. Lienau. Quantum coherence controls the charge separation in a prototypical artificial light-harvesting system. *Nature Communications*, 4:1602, 2013.
- [78] R. Noriega, J. Rivnay, K. Vandewal, F. P. V. Koch, N. Stingelin, P. Smith, M. F. Toney and A. Salleo. A general relationship between disorder, aggregation and charge transport in conjugated polymers. *Nature Materials*, 12:1038-1044, 2013.
- [79] James B. Foresman, Martin Head-Gordon, John A. Pople and Michael J Frisch. Toward a Systematic Molecular Orbital Theory for Excited States. *Journal of Physical Chemistry*, 96:135-149, 1992.
- [80] P. G. Lykos, R. G. Parr. On the pi-electron approximation and its possible refinement. *Journal of Chemical Physics*, 24:1166, 1956.
- [81] Lobaugh John and Rossky J. Peter. Solvent and intramolecular effects on the absorption spectrum of betaine-30. *Journal of Physical Chemistry A*, 104:899, 2000.

- [82] Muller P. Richard and Warshel Arieh. Ab initio calculations of free energy barriers for chemical reactions in solution. *Journal of Physical Chemistry*, 99:17516, 1995.
- [83] Johannes Gierschner, Hans-Georg Mack, Larry Luer, and Dieter Oelkrug. Fluorescence and absorption spectra of oligophenylenevinyls: Vibronic coupling band shapes, and solvatochromism. *Journal of Physical Chemistry C*, 114:5182-5186, 2010.